Wavelet analysis of covariance with application to atmospheric time series

Brandon Whitcher

EURANDOM, P.O. Box 513, 5600 MB Eindhoven, The Netherlands.

Peter Guttorp

University of Washington, Department of Statistics, Box 354322, Seattle, WA

98195-4322, USA.

Donald B. Percival

University of Washington, Applied Physics Laboratory, Box 355640, Seattle, WA

98195-5640, USA; and MathSoft, Inc., 1700 Westlake Avenue North, Seattle,

Washington 98109-9891, USA.

Short title: WAVELET ANALYSIS OF COVARIANCE

Abstract. Multi-scale analysis of univariate time series has appeared in the literature at an ever increasing rate. Here we introduce the multi-scale analysis of covariance between two time series using the discrete wavelet transform. The wavelet covariance and wavelet correlation are defined and applied to this problem as an alternative to traditional cross-spectrum analysis. The wavelet covariance is shown to decompose the covariance between two stationary processes on a scale by scale basis. Asymptotic normality is established for estimators of the wavelet covariance and correlation. Both quantities are generalized into the wavelet cross-covariance and cross-correlation in order to investigate possible lead/lag relationships. A thorough analysis of interannual variability for the Madden–Julian oscillation is performed using a 35+ year record of daily station pressure series. The time localization of the discrete wavelet transform allows the sub-series, which are associated with specific physical time scales, to be partitioned into both seasonal periods (such as summer and winter) and also according to El-Niño–Southern Oscillation (ENSO) activity. Differences in variance and correlation between these periods may then be firmly established through statistical hypothesis testing. The daily station pressure series used here show clear evidence of increased variance and correlation in winter across Fourier periods of 16–128 days. During warm episodes of ENSO activity, a reduced variance is observed across Fourier periods of 8–512 days for the station pressure series from Truk Island and little or no correlation between station pressure series for the same periods.

Some key words: Confidence intervals; Cross-correlation; Cross-covariance; Madden–Julian oscillation; Maximal overlap discrete wavelet transform; Southern Oscillation Index.

1. Introduction

The bivariate relationship between two time series is often of crucial interest in atmospheric science. For example, the Madden–Julian oscillation (MJO) [*Madden and Julian*, 1971] was found using bivariate spectral analysis between the station pressure and zonal wind components at Canton Island (2.8°S, 171.7°W) – specifically the co-spectrum and magnitude squared coherence. This oscillation has been documented as having a period anywhere from 30–60 days and has appeared in many studies in the Indian Ocean and tropical Pacific Ocean; see *Madden and Julian* [1994] for a review. Several empirical studies, using a wide variety of atmospheric time series, have noted a time-varying aspect to the oscillation. Its apparent broadband nature might be best described as non-stationary in a statistical sense; i.e., the mean or variance of these observed time series vary with time. The broad peak observed in previous spectral analyses might be attributed to modulation in frequency and/or amplitude of the oscillation over the measured time series.

Given the potential time-varying nature of the MJO, as observed through atmospheric time series, analyzing it using a transform which captures events both locally in time and frequency is appealing. The short-time Fourier transform is one such technique, where the discrete Fourier transform is applied to subsets of the time series via a moving window resulting in a grid-like partition of the time-frequency plane. The discrete wavelet transform (DWT) is another technique, where the time-frequency plane is partitioned such that high-frequencies are given small windows in time and low-frequencies are given large windows in time via an adaptive windowing of the time series. See *Kumar and Foufoula-Georgiou* [1994] and *Kumar* [1996] for descriptions of time-frequency/time-scale analysis in a geophysical setting. A non-decimated version of the orthonormal DWT – the maximal overlap DWT (MODWT) – has proven useful in analyzing various geophysical processes [*Percival and Guttorp*, 1994; *Percival and Mofjeld*, 1997].

It is known that the wavelet variance, for a univariate time series, is an alternative representation of the spectral density function (SDF) for stationary and certain types of non-stationary processes [*Percival*, 1995]. The adaptive windowing (band-pass filtering) by the DWT produces wavelet coefficients associated with specific frequency intervals instead of individual frequencies as are Fourier coefficients in the periodogram. A key advantage over the periodogram is that the wavelet variance involves basis functions that are local in time – allowing for non-stationary features to be characterized by the wavelet variance. Here, we introduce the wavelet covariance and correlation between two processes. They are alternative representations of the cross spectrum and magnitude squared coherence, respectively, that allow for levels of association between time series to vary over time.

Previous investigations of the MJO have used classical and ad-hoc Fourier-based techniques to measure possible time-varying association between atmospheric time series without the ability to rigorously test for differences between disjoint time periods (see Section 1.1). Some previous studies, such as Anderson *et al.* [1984] and *Madden* [1986], designed custom filters and then explicitly band-pass filter their observed time series in order to analyze its time-varying structure. Instead of having to design a specific set of filters, the DWT provides a convenient collection of band-pass filters whose inherent structure allows for relatively straightforward manipulation of its output (wavelet coefficients) into recognizable statistical quantities such as variance, covariance and correlation.

For example, one quantity of interest might be the correlation between the MJO and Southern Oscillation Index (SOI) around the standard periods of the MJO, 32–64 days. A possible hypothesis to test is: are the MJO and SOI associated in boreal winter and boreal summer? Looking at Figure 8, the wavelet correlation for wavelet scale 16 (corresponding to Fourier periods of 32–64 days) is not significantly different from zero in boreal summer (-0.08 with approximate 95% confidence interval of $[-0.15, 0.04]$) and

is greater than zero in boreal winter (0.38 with approximate 95% confidence interval of $[0.30, 0.46]$). The fact that these two confidence intervals do not overlap is equivalent to rejecting the null hypothesis of equivalent levels of association at an $\alpha < 0.05$ level of significance. A much more thorough analysis between these time series is presented in Section 5. We will show that wavelet-based techniques allow one to make quantitative statements about variables of interest where only qualitative comparisons were available in the past. A review of previous investigations concerning the time-varying nature of the MJO follows, along with a review of the small amount of literature concerning bivariate wavelet methodology and a brief outline of this paper.

1.1. Previous Work on the Madden–Julian Oscillation

Temporal variations in the MJO and its relationship with El Niño–Southern Oscillation (ENSO) events have previously been investigated using techniques such as cross-spectral analysis. Previous work on the time-varying nature of the MJO includes *Madden* [1986] who performed a seasonally varying cross-spectral analysis on nearly twenty time series of rawinsonde data from tropical stations around the world. The MJO appears strongest during December–February (boreal winter) and weakest during June–August (boreal summer), and that it is always stronger in the western Pacific and Indian oceans than elsewhere. *Gutzler* [1991] used daily time series from six near-equatorial rawinsonde stations to investigate intraseasonal variance of zonal winds (200 and 850 mb) . Interannual modulation of the amplitude of the MJO was observed at stations east of 140°E (which includes Truk Island) and the 31–66 day variance was observed to increase in the lower troposphere during warms events, as indicated by the Southern Oscillation. *Salby and Hendon* [1994] found a much broader spectral peak of 35–95 days in convection along the equator, rather than the 30–60 day band as in *Madden* [1986]. *Madden and Julian* [1994] noted the broadband nature of the oscillation by comparing the station pressure spectra for Truk Island (7.4°N, 151.8°W) during two

time spans – 1967 to 1979 and 1980 to 1985. The MJO appeared to have a 26-day period in the early 1980s.

The influence of ENSO events has also been hypothesized to affect characteristics of the MJO. Anderson *et al.* [1984] filtered atmospheric relative angular momentum (4 years) and the 850–200 mb shear of the zonal wind at Truk Island (25 years) with a filter designed to pass the frequency band corresponding to periods of 32–64 days. They noted that, with respect to the Truk Island series, a possible association with increased amplitude of the oscillation during the 1956–57, 1972–73, and 1976–77 ENSO warm events but noted that the duration of these increases were much longer than the ENSO events. *Gray* [1988] performed a correlation analysis between daily station pressure data from Truk (7°N, 152°W), Balboa (9°N, 80°W), Darwin (12°S, 131°E) and Gan (1°S, 73°E), with seasonal sea surface temperature anomalies on a 5° grid. The data were partitioned into ENSO and non-ENSO years; in non-ENSO years a strong seasonal shift in frequency was found at all sites except Truk Island.

Kuhnel [1989] investigated the characteristics of a 40–50 day oscillation in cloudiness for the Australo–Indonesian region. Using data on a $10° \times 5°$ grid, regions in the eastern Indian Ocean and western Pacific Ocean were found to have a pronounced 40–50 day peak with no obvious seasonal variation. Another region in the Indian Ocean (5–15°S, 95–100°E) showed a stronger oscillation in the March–June period. Regions around 5–15°S over northern Australia and in the Pacific Ocean showed a much stronger 40–50 day oscillation during the Australian monsoon season from December to March than the rest of the year. The 40–50 day cloud amount oscillation did not appear to be affected by warm ENSO events. *Murakami and Sumathipala* [1989] looked for synoptic scale 'westerly bursts' over the western Pacific ocean and their possible influence on the 1982–83 ENSO. Analyzing daily 850 mb winds, along with daily OLR and SST data, they utilized a type of multiresolution analysis via bandpass filtering and also partitioned the filtered series into summer and winter seasons. Only loose associations

were found between interannual modes and the number of days of westerly acceleration, although strong associations in air-sea interactions occurred during heightened ENSO activity.

Weickmann [1991] looked at ENSO and the MJO during 1981–82 using outgoing longwave radiation (OLR). Some similarity was found between the MJO and its transients, and the December 1981 ENSO-related transition and its transients. *Gambis* [1992] applied the continuous wavelet transform (CWT) to the derived length of day (LOD) and Southern Oscillation Index, where the LOD exhibits 50–55 day oscillations similar to those observed in the MJO. Increased numbers of significant high-frequency bands were observed during the northern hemisphere winters. However, high-frequency content ($\approx$ 55 day period) in the LOD did not appear to be more concentrated during El Niño events, but a strong concentration of low-frequency ($\approx$ 1000–3000 day period) oscillations did correspond to ENSO events. For the SOI, both low- and high-frequency content were more concentrated during El Niño events. No hypothesis testing was performed, nor was any attempt made to perform a bivariate wavelet analysis.

Anyamba and Weare [1995] sought to better define year-to-year variability, propagation properties and spatial structure of the 40–50 day oscillation. An autoregressive spectrum (with order varying between 10 and 25 terms) was fit to OLR, spatially smoothed onto a $5° \times 5°$ grid, with several higher-frequency spectral peaks being visually significant. The MJO tended to be weaker in amplitude during July-August (as in *Madden* [1986]) because of a shift away from the equator by the dominant spatial mode. Suppression of the MJO appeared to occur during the entire 1982–83 ENSO episode. Kestin *et al.* [1998] used three time-frequency techniques to examine the variance structure of ENSO; applying them to the SOI, sea surface temperature series (Niño 3) and tropical Pacific rainfall index. Interannual variability of ENSO is contained in a 2–10 year period and not distributed uniformly over time. The time-frequency patterns are similar for all three time series, particularly between

the SOI and sea surface temperature series. Hendon *et al.* [1999] investigated the year-to-year variations of the MJO and its interaction with ENSO. Interannual variation of the level of MJO activity was observed to occur independently of ENSO, except for exceptional warm events when MJO activity appeared to be drastically diminished.

1.2. Previous Work on Bivariate Wavelet Techniques

The ability of the DWT to capture variability in both time and scale can provide insight into the nature of atmospheric phenomena such as the MJO, but we must make use of the DWTs of two time series in such a way that these bivariate properties can be brought out. *Hudgins* [1992] introduced the concepts of the wavelet cross spectrum and wavelet cross correlation in terms of the CWT. In a subsequent paper, Hudgins *et al.* [1993] applied these concepts to atmospheric turbulence. They found the bivariate wavelet techniques provided a better analysis of the data over traditional Fourier methods – especially at low frequencies. *Liu* [1994] defined a cross wavelet spectrum, equivalent to that of *Hudgins* [1992], and complex-valued wavelet coherency which was constructed using the co- and quadrature wavelet spectra. These quantities were used to reveal new insights on ocean wind waves such as wave group parameterizations, phase relations, and wave breaking characteristics.

Lindsay *et al.* [1996] defined the sample wavelet covariance for the DWT and MODWT along with confidence intervals based on large sample results. They applied this methodology to the surface temperature and albedo of ice pack in the Beaufort Sea. Recently, *Torrence and Compo* [1998] discussed the cross-wavelet spectrum, which is complex valued, and the cross-wavelet power, which is the magnitude of their cross-wavelet spectrum, in terms of the CWT. They also introduced confidence intervals for their cross-wavelet power and compared the SOI with Niño3 sea surface temperature readings.

In this paper, we extend the notion of wavelet covariance for the maximal overlap

DWT and define the wavelet cross-covariance and wavelet cross-correlation. The wavelet cross-covariance is shown to decompose the process cross-covariance on a scale by scale basis for specific types of non-stationary stochastic processes. Asymptotic normality is obtained for the MODWT-based estimators of wavelet cross-covariance.

1.3. Outline

The MODWT, a non-decimated variation of the DWT, is described in Section 2. In Section 3, the wavelet cross-covariance and cross-correlation are defined in terms of the MODWT coefficients at a particular scale of the transform. Central limit theorems are provided for estimators of both quantities based on a finite sample of MODWT coefficients (for completeness the proofs are provided in a separate technical report: Whitcher *et al.* [1999]). Explicit methods for computing approximate $100(1 - 2p)\%$ confidence intervals are provided in Section 4. Fisher's z-transformation is utilized in order to keep the confidence interval of the wavelet correlation bounded by ± 1 for small sample sizes.

In Section 5, we perform a wavelet analysis of covariance with a daily Southern Oscillation Index and daily station pressure measurements from Truk Island. Spectral analysis shows two peaks in the magnitude squared coherence between the two time series around the established MJO range of frequencies, and cross-correlation analysis provides a complicated correlation structure. A wavelet analysis of variance and correlation is performed where the data is partitioned into seasons (boreal summer and winter) and episodes of ENSO activity (warm, cold and other). Hypothesis testing highlights the differences between these time series across a variety of physical time scales.

2. Maximal Overlap Discrete Wavelet Transform

The DWT of a time series $\mathbf{X}$ is now a reasonably well-established method for analyzing its multi-scale features. In this section we provide a brief introduction to a variation of the orthonormal DWT, called the maximal overlap DWT (MODWT). The MODWT gives up orthogonality (through not subsampling) in order to gain features such as translation-invariance and the ability to analyze a time series with arbitrary sample size. Here, we follow previous definitions of the MODWT by *Percival and Guttorp* [1994] and *Percival and Mofjeld* [1997].

Let $\{\tilde{h}_1\} \equiv \{\tilde{h}_{1,0}, \ldots, \tilde{h}_{1,L-1}\}$ denote the wavelet filter coefficients from a Daubechies compactly supported wavelet family [*Daubechies*, 1992, Sec. 6.2] and let $\{\tilde{g}_1\} \equiv \{\tilde{g}_{1,0}, \ldots, \tilde{g}_{1,L-1}\}$ be the corresponding scaling filter coefficients, defined via the quadrature mirror relationship $\tilde{g}_{1,m} = (-1)^{m+1}\tilde{h}_{1,L-1-m}$. By definition, the wavelet filter $\{\tilde{h}_1\}$ is associated with unit scale, is normalized such that $\sum \tilde{h}_l^2 = 1/2$ and is orthogonal to its even shifts. For any sample size $N \geq L$ and with $h_{1,m} = 0$ for $m \geq L$, let

$$\widetilde{H}_{1,k} = \sum_{m=0}^{N-1} \tilde{h}_{1,m}\, e^{-i2\pi mk/N}, \quad k = 0, \ldots, N-1,$$

be the discrete Fourier transform (DFT) of $\{\tilde{h}_1\}$, and let $\widetilde{G}_{1,k}$ denote the DFT of $\{\tilde{g}_1\}$. Now define the wavelet filter $\{\tilde{h}_j\}$ for scale $\lambda_j \equiv 2^{j-1}$ as the inverse DFT of

$$\widetilde{H}_{j,k} = \widetilde{H}_{1,2^{j-1}k \bmod N} \prod_{l=0}^{j-2} \widetilde{G}_{1,2^l k \bmod N}, \quad k = 0, \ldots, N-1. \tag{1}$$

The wavelet filter associated with scale λ_j has length $\min\{N, L_j\}$ where $L_j \equiv (2^j - 1)(L - 1) + 1$. Also, define the scaling filter $\{\tilde{g}_J\}$ for scale $2\lambda_J$ as the inverse DFT of

$$\widetilde{G}_{J,k} = \prod_{l=0}^{J-1} \widetilde{G}_{1,2^l k \bmod N}, \quad k = 0, \ldots, N-1. \tag{2}$$

In order to construct a jth order partial MODWT, we let $\{\mathcal{X}_k\} \equiv \{\mathcal{X}_0, \ldots, \mathcal{X}_{N-1}\}$ be the DFT of $\mathbf{X}$ (for arbitrary N). The vector of MODWT coefficients $\widetilde{\mathbf{W}}_j$, $j = 1, \ldots, J$

is defined to be the inverse DFT of $\{\widetilde{H}_{j,k}\mathcal{X}_k\}$ and is associated with changes of scale λ_j. The vector of MODWT scaling coefficients $\widetilde{\mathbf{V}}_J$ is defined similarly by the inverse DFT of $\{\widetilde{G}_{J,k}\mathcal{X}_k\}$ and is associated with averages of scale $2\lambda_J$ and higher. For time series of dyadic length, the MODWT may be subsampled and rescaled to obtain an orthonormal DWT. In practice, a pyramid scheme similar to that of the DWT is utilized to compute the MODWT; see *Percival and Guttorp* [1994] and *Percival and Mofjeld* [1997].

The MODWT coefficients may be interpreted as differences of weighted averages from the original observations. To better understand this statement let us consider the Haar scaling (low-pass) filter. For unit scale $j = 1$, the Haar scaling filter has length two with values $\{1/\sqrt{2}, 1/\sqrt{2}\}$, and hence, when applied to a time series, yields an output that is proportional to a simple average of two observations. Applying Equation (2) for arbitrary j and taking the inverse DFT, we obtain filters whose output are proportional to simple averages of 2^j observations. For all scales, the corresponding wavelet filter is orthogonal to the scaling filter: its coefficients have the same magnitudes, but the first half are negative, thus forming differences of averages each of length 2^{j-1}. Using an accepted measure of 'equivalent width,' all Daubechies scaling filters $\{\tilde{g}_{j,l}\}$ have the same width as the Haar [*Percival and Walden*, 2000, Sec. 4.6]. Since the corresponding wavelet filters are again orthogonal to the scaling filters, the wavelet coefficients essentially capture the difference between two weighted averages, each over half the length of the Haar scaling filter.

The structure of the MODWT utilizes approximate ideal band-pass filters with pass-band given by the range of frequencies $[1/2^{j+1}, 1/2^j)$ for scales $1 \leq j \leq J$. The accuracy of the approximation improves as the length of the wavelet filter increases. Inverting the frequency range to produce a period of time, and multiplying by the appropriate time units Δt, we obtain the equivalent periods of $[2^j, 2^{j+1}] \Delta t$ days for scales $1 \leq j \leq J$. In order to help relate wavelet coefficients to the physical processes they are analyzing, we will give both the wavelet scale and Fourier period when

discussing results.

Percival and Mofjeld [1997] proved that the MODWT is an energy preserving transform in the sense that

$$\|\mathbf{X}\|^2 = \sum_{j=1}^{J} \|\widetilde{\mathbf{W}}_j\|^2 + \|\widetilde{\mathbf{V}}_J\|^2.$$

This allows for a scale-based analysis of variance of a time series similar to spectral analysis via the DFT. In a wavelet analysis of variance, the individual wavelet coefficients are associated with a band of frequencies and specific time scale whereas Fourier coefficients are associated with a specific frequency only.

3. Wavelet-Based Estimators of Covariance and Correlation

Here we define the basic quantities of interest for estimating association between two time series using the MODWT. The decomposition of covariance on a scale by scale basis of the wavelet covariance is shown, and central limit theorems are provided for the wavelet covariance and correlation.

3.1. Definition and Properties of the Wavelet Cross-Covariance

Let $\{U_t\} \equiv \{\ldots, U_{-1}, U_0, U_1, \ldots\}$ be a stochastic process whose dth order backward difference $(1 - B)^d U_t = Z_t$ is a stationary Gaussian process with zero mean and spectral density function $S_Z(\cdot)$, where d is a non-negative integer. Let

$$\overline{W}_{j,t}^{(U)} = \tilde{h}_{j,l} * U_t \equiv \sum_{l=0}^{L_j - 1} \tilde{h}_{j,l} U_{t-l}, \quad t = \ldots, -1, 0, 1, \ldots,$$

be the stochastic process obtained by filtering $\{U_t\}$ with the MODWT wavelet filter $\{\tilde{h}_{j,l}\}$. *Percival and Walden* [2000, Sec. 8.2] showed that if $L \geq 2d$, then $\{\overline{W}_{j,t}^{(U)}\}$ is a stationary process with zero mean and spectrum given by $S_{j,U}(\cdot)$.

Let $\{X_t\} \equiv \{\ldots, X_{-1}, X_0, X_1, \ldots\}$ and $\{Y_t\} \equiv \{\ldots, Y_{-1}, Y_0, Y_1, \ldots\}$ be stochastic processes whose d_Xth and d_Yth order backward differences are stationary Gaussian

processes as defined above, and define $d \equiv \max\{d_X, d_Y\}$. Let $S_{XY}(\cdot)$ denote their cross spectrum and, $S_X(\cdot)$ and $S_Y(\cdot)$ denote their autospectra, respectively. The wavelet cross-covariance of $\{X_t, Y_t\}$ for scale $\lambda_j = 2^{j-1}$ and lag τ is defined to be

$$\gamma_{\tau,XY}(\lambda_j) \equiv \mathrm{Cov}\left\{\overline{W}_{j,t}^{(X)}, \overline{W}_{j,t+\tau}^{(Y)}\right\}, \tag{3}$$

where $\{\overline{W}_{j,t}^{(X)}\}$ and $\{\overline{W}_{j,t}^{(Y)}\}$ are the scale λ_j MODWT coefficients for $\{X_t\}$ and $\{Y_t\}$, respectively. The MODWT coefficients have mean zero, when $L \geq 2d$, and therefore $\gamma_{\tau,XY}(\lambda_j) = E\{\overline{W}_{j,t}^{(X)}\overline{W}_{j,t+\tau}^{(Y)}\}$. When $\tau = 0$ we obtain the wavelet covariance between $\{X_t, Y_t\}$, which we denote as $\gamma_{XY}(\lambda_j) = \gamma_{0,XY}(\lambda_j)$ to simplify notation.

Setting $\tau = 0$ and Y_t to X_t or X_t to Y_t, Equation (3) reduces to the wavelet variance for X_t or Y_t denoted as, respectively, $\nu_X^2(\lambda_j)$ or $\nu_Y^2(\lambda_j)$ [*Percival*, 1995]. The wavelet variance decomposes the process variance on a scale by scale basis, and the wavelet cross-covariance give a similar decomposition for the process cross-covariance. To be precise, let $\{X_t\}$ and $\{Y_t\}$ be two weakly stationary processes with autospectra given by $S_X(f)$ and $S_Y(f)$, respectively. If we require $L > 2d$, then for any integer $J \geq 1$ we have

$$C_{\tau,XY} \equiv \mathrm{Cov}\{X_t, Y_{t+\tau}\} = \mathrm{Cov}\left\{\overline{V}_{J,t}^{(X)}, \overline{V}_{J,t+\tau}^{(Y)}\right\} + \sum_{j=1}^{J} \gamma_{\tau,XY}(\lambda_j),$$

where $\overline{V}_{J,t}^{(X)} \equiv \tilde{g}_{J,l} * X_t$ and $\overline{V}_{J,t}^{(Y)} \equiv \tilde{g}_{J,l} * Y_t$ are obtained by filtering $\{X_t\}$ and $\{Y_t\}$ using the MODWT scaling filter $\{\tilde{g}_{J,l}\}$, respectively. As $J \to \infty$, we have

$$C_{\tau,XY} = \sum_{j=1}^{\infty} \gamma_{\tau,XY}(\lambda_j), \tag{4}$$

which gives the required decomposition [Whitcher *et al.* 1999]. If we think of $\{\tilde{g}_J\}$ as a low-pass filter covering the nominal frequency band $[-2^{-(J+1)}, 2^{-(J+1)}]$, this statement is intuitively plausible since the scaling filter $\{\tilde{g}_J\}$ is capturing smaller and smaller portions of the cross spectrum as $J \to \infty$.

3.2. Estimating the Wavelet Cross-Covariance

Suppose $X_0, \dots, X_{N-1}$ and $Y_0, \dots, Y_{N-1}$ can be regarded as realizations of portions of the processes $\{X_t\}$ and $\{Y_t\}$, whose d_Xth and d_Yth order backward differences form stationary Gaussian processes. As before, let $d = \max\{d_X, d_Y\}$.

Let $\widetilde{W}_{j,t} = \overline{W}_{j,t}$ for those indices t where $\widetilde{W}_{j,t}$ is unaffected by the boundary – this is true as long as $t \geq L_j - 1$. Thus, if $N \geq L_j$, we can define a biased estimator $\tilde{\gamma}_{\tau,XY}(\lambda_j)$ of the wavelet cross-covariance based upon the MODWT via

$$
\tilde{\gamma}_{\tau,XY}(\lambda_j) \equiv \begin{cases} \widetilde{N}_j^{-1} \sum_{l=L_j-1}^{N-\tau-1} \widetilde{W}_{j,l}^{(X)} \widetilde{W}_{j,l+\tau}^{(Y)}, & \tau = 0, \dots, \widetilde{N}_j - 1; \\ \widetilde{N}_j^{-1} \sum_{l=L_j-1-\tau}^{N-1} \widetilde{W}_{j,l}^{(X)} \widetilde{W}_{j,l+\tau}^{(Y)}, & \tau = -1, \dots, -(\widetilde{N}_j - 1); \\ 0, & \text{otherwise}, \end{cases}
$$

where $\widetilde{N}_j \equiv N - L_j + 1$. The bias is due to the denominator $1/\widetilde{N}_j$ remaining constant for all lags, though it disappears at lag $\tau = 0$. Let us now state the large sample properties of the wavelet covariance estimator; i.e., $\tilde{\gamma}_{XY}(\lambda_j) \equiv \tilde{\gamma}_{0,XY}(\lambda_j)$ (see Whitcher et al. [1999] for proofs).

If $L > 2d$, and suppose $\{\overline{W}_{j,t}^{(X)}, \overline{W}_{j,t}^{(Y)}\}$ is a bivariate Gaussian stationary process with autospectra satisfying $\int_{-1/2}^{1/2} S_{j,X}^2(f) < \infty$ and $\int_{-1/2}^{1/2} S_{j,Y}^2(f) < \infty$, then

$$
\tilde{\gamma}_{XY}(\lambda_j) \sim N\left(\gamma_{XY}(\lambda_j), \widetilde{N}_j^{-1} S_{j,(XY)}(0)\right); \tag{5}
$$

i.e., the MODWT-based estimator of wavelet covariance is normally distributed with mean $\gamma_{XY}(\lambda_j)$ and large sample variance $\widetilde{N}_j^{-1} S_{j,(XY)}(0)$. The quantity $S_{j,(XY)}(0)$ is the spectral density function for $\{\overline{W}_{j,t}^{(X)} \overline{W}_{j,t}^{(Y)}\}$ (the product of the scale λ_j MODWT coefficients) at zero frequency. We may generalize to the wavelet cross-covariance by simply replacing shifting $\{\overline{W}_{j,t}^{(Y)}\}$ with respect to $\{\overline{W}_{j,t}^{(X)}\}$ and appealing to the same result.

Because of the Gaussian assumption, we can obtain an expression for $S_{j,(XY)}(0)$ in

Equation (5) in terms of auto- and cross spectra for large $\widetilde{N}_j$, namely

$$\mathcal{V}_j \equiv S_{j,(XY)}(0) = \int_{-1/2}^{1/2} S_{j,X}(f)S_{j,Y}(f)\, df + \int_{-1/2}^{1/2} S_{j,XY}^2(f)\, df. \tag{6}$$

Note carefully that $S_{j,XY}(f)$ is the cross spectrum between two series of scale λ_j MODWT coefficients whereas $S_{j,(XY)}(f)$ is the autospectrum for the product of scale λ_j MODWT coefficients. The result in Equation (5) allows us to easily construct approximate confidence intervals for the MODWT-based estimator of the wavelet covariance.

3.3. Wavelet Cross-Correlation

We can define the wavelet cross-correlation for scale λ_j and lag τ as

$$\rho_{\tau,XY}(\lambda_j) \equiv \frac{\mathrm{Cov}\left\{\overline{W}_{j,t}^{(X)}, \overline{W}_{j,t+\tau}^{(Y)}\right\}}{\left(\mathrm{Var}\left\{\overline{W}_{j,t}^{(X)}\right\}\mathrm{Var}\left\{\overline{W}_{j,t+\tau}^{(Y)}\right\}\right)^{1/2}} = \frac{\gamma_{\tau,XY}(\lambda_j)}{\nu_X(\lambda_j)\nu_Y(\lambda_j)}.$$

Since this is just a correlation coefficient between two random variables, $-1 \leq \rho_{\tau,XY}(\lambda_j) \leq 1$ for all τ, j. The wavelet cross-correlation is roughly analogous to its Fourier counterpart – the magnitude squared coherence – but it is related to bands of frequencies (scales). Just as the cross-correlation is used to determine lead/lag relationships between two processes, the wavelet cross-correlation will provide a lead/lag relationship on a scale by scale basis.

3.4. Estimating the Wavelet Cross-Correlation

Since the wavelet cross-correlation is simply made up of the wavelet cross-covariance for $\{X_t, Y_t\}$ and wavelet variances for $\{X_t\}$ and $\{Y_t\}$, the MODWT estimator of the wavelet cross-correlation is simply

$$\tilde{\rho}_{\tau,XY}(\lambda_j) \equiv \frac{\tilde{\gamma}_{\tau,XY}(\lambda_j)}{\tilde{\nu}_X(\lambda_j)\tilde{\nu}_Y(\lambda_j)}, \tag{7}$$

where $\tilde{\gamma}_{\tau,XY}(\lambda_j)$ is the wavelet covariance, and $\tilde{\nu}_X^2(\lambda_j)$ and $\tilde{\nu}_Y^2(\lambda_j)$ are the wavelet variances. When $\tau = 0$ we obtain the MODWT estimator of the wavelet correlation between $\{X_t, Y_t\}$, denoted as $\tilde{\rho}_{XY}(\lambda_j)$ for simplicity.

Large sample theory for the cross-correlation is more difficult to come by than for the cross-covariance. *Brillinger* [1979] constructed approximate confidence intervals for the auto and cross-correlation sequences of bivariate stationary time series. We use his technique to establish a central limit theorem for the MODWT estimated wavelet cross-correlation in Whitcher *et al.* [1999]. To simplify notation the following gives a central limit theorem for the wavelet correlation ($\tau = 0$) but easily generalizes to arbitrary lags.

Let $L > 2d$, and suppose $\{\overline{W}_{j,t}^{(X)}, \overline{W}_{j,t}^{(Y)}\}$ is a bivariate Gaussian stationary process with square integrable autospectra, then

$$\tilde{\rho}_{XY}(\lambda_j) \sim N\left(\rho_{XY}(\lambda_j), \widetilde{N}_j^{-1} R_j\right); \tag{8}$$

i.e., the MODWT-based estimator $\tilde{\rho}_{XY}(\lambda_j)$ of the wavelet correlation is asymptotically normally distributed with mean $\rho_{XY}(\lambda_j)$ and large sample variance given by

$$
\begin{aligned}
R_j \equiv \mathrm{Var}\{\tilde{\rho}_{XY}(\lambda_j)\} \quad \approx \quad & \frac{1}{\widetilde{N}_j} \sum_{\tau=-(\widetilde{N}_j-1)}^{\widetilde{N}_j-1} \{\, \rho_{\tau,X}(\lambda_j)\rho_{\tau,Y}(\lambda_j) + \rho_{\tau,XY}(\lambda_j)\rho_{\tau,YX}(\lambda_j) \\
& - 2\rho_{0,XY}(\lambda_j)[\rho_{\tau,X}(\lambda_j)\rho_{\tau,YX}(\lambda_j) + \rho_{\tau,Y}(\lambda_j)\rho_{\tau,YX}(\lambda_j)] \\
& + \rho_{0,XY}^2(\lambda_j)[\tfrac{1}{2}\rho_{\tau,X}^2(\lambda_j) + \rho_{\tau,XY}^2(\lambda_j) + \tfrac{1}{2}\rho_{\tau,Y}^2(\lambda_j)] \,\},
\end{aligned}
$$

where $\rho_{\tau,X}(\lambda_j) \equiv E\{\overline{W}_{j,t}^{(X)}\overline{W}_{j,t+|\tau|}^{(X)}\}/[2\lambda_j\nu_X^2(\lambda_j)]$ is the scale λ_j wavelet autocorrelation for the process $\{X_t\}$.

4. Confidence Intervals for Wavelet Estimators

With central limit theorems for both the wavelet cross-covariance and cross-correlation, we may now explicitly construct an approximate confidence interval (CI) for

the estimators. For the wavelet cross-correlation, a nonlinear transformation is utilized in order to bound it between ± 1 and reduce the computational complexity of its large sample variance. Without loss of generality, we provide the following CIs for lag $\tau = 0$. We may generalize the results presented here for arbitrary lag by simply replacing $\{\widetilde{W}_{j,t}^{(X)}\}$ and $\{\widetilde{W}_{j,t}^{(Y)}\}$ with $\{\widetilde{W}_{j,t}^{(X)}\}$ where $t = L_j + \tau - 1, ..., N - 1$ and $\{\widetilde{W}_{j,t+\tau}^{(Y)}\}$ where $t = L_j - 1, ..., N - \tau - 1$ for $\tau \geq 0$, or $\{\widetilde{W}_{j,t}^{(X)}\}$ where $t = L_j - 1, ..., N + \tau - 1$ and $\{\widetilde{W}_{j,t+\tau}^{(Y)}\}$ where $t = L_j - \tau - 1, ..., N - 1$ for $\tau < 0$.

4.1. Wavelet Cross-covariance

The formula for an approximate $100(1 - 2p)\%$ CI of the scale λ_j MODWT estimator of the wavelet cross-covariance $\tilde{\gamma}_{\tau,XY}(\lambda_j)$, starting from Equation (6), is provided; see also Lindsay *et al.* [1996]. We make use of the periodogram and the cross-periodogram to help estimate quantities of interest under the assumption of $\tau = 0$. First, we use the periodogram $\widehat{S}_{j,X}^{(p)}(\cdot)$ of $\{\widetilde{W}_{j,t}^{(X)}\}$ as the estimator of $S_{j,X}(\cdot)$, and similarly for $\widehat{S}_{j,Y}^{(p)}(\cdot)$ of $\{\widetilde{W}_{j,t}^{(Y)}\}$. Next, we define the biased estimator of the autocovariance sequence associated with the scale λ_j MODWT coefficients of $\{X_t\}$ by

$$\hat{s}_{j,m,X}^{(p)} \equiv \frac{1}{\widetilde{N}_j} \sum_{l=L_j-1}^{N-1-|m|} \widetilde{W}_{j,l}^{(X)} \widetilde{W}_{j,l+|m|}^{(X)},$$

A similar definition applies to $\{\hat{s}_{j,m,Y}^{(p)}\}$, the biased estimator of the autocovariance sequence associated with the scale λ_j MODWT coefficients $\{\widetilde{W}_{j,t+m}^{(Y)}\}$. Second, we use the cross-periodogram $\widehat{S}_{j,XY}^{(p)}(\cdot)$ of $\{\widetilde{W}_{j,t}^{(X)}\}$ and $\{\widetilde{W}_{j,t}^{(Y)}\}$, as the estimator of $S_{j,XY}(\cdot)$, and the corresponding biased estimator of the cross covariance sequence associated with the scale λ_j MODWT coefficients by

$$\widehat{C}_{j,m,XY}^{(p)} \equiv \frac{1}{\widetilde{N}_j} \sum_{l} \widetilde{W}_{j,l}^{(X)} \widetilde{W}_{j,l+m}^{(Y)},$$

where the summation goes from $l = L_j - 1, \ldots, N - m - 1$ for $m \geq 0$ and from $l = L_j - m - 1, \ldots, N - 1$ for $m < 0$.

We can use Parseval's relation to develop an estimate of the large sample variance for the MODWT-based estimator of the wavelet cross-covariance (Equation (6)) using the autocovariance and cross-covariance sequences of the MODWT coefficients. Specifically, the integral of the product of the periodograms is determined from the autocovariance sequences of $\{\widetilde{W}_{j,t}^{(X)}\}$ and $\{\widetilde{W}_{j,t}^{(Y)}\}$ via

$$\int_{-1/2}^{1/2} \widehat{S}_{j,X}^{(p)}(f)\widehat{S}_{j,Y}^{(p)}(f)\,df = \hat{s}_{j,0,X}^{(p)}\hat{s}_{j,0,Y}^{(p)} + 2\sum_{m=1}^{\widetilde{N}_j-1} \hat{s}_{j,m,X}^{(p)}\hat{s}_{j,m,Y}^{(p)},$$

and the integral of the squared cross periodogram from the cross covariance sequence of $\{\widetilde{W}_{j,t}^{(X)}, \widetilde{W}_{j,t}^{(Y)}\}$ via

$$\int_{-1/2}^{1/2} \left[\widehat{S}_{j,YX}^{(p)}(f)\right]^2\,df = \sum_{m=-(\widetilde{N}_j-1)}^{\widetilde{N}_j-1} \left[\widehat{C}_{j,m,XY}^{(p)}\right]^2.$$

Hence, an estimate for the large sample variance of the MODWT estimator of the wavelet cross-covariance is given by

$$\widetilde{\mathcal{V}}_j \equiv \frac{\hat{s}_{j,0,X}^{(p)}\hat{s}_{j,0,Y}^{(p)}}{2} + \sum_{m=1}^{\widetilde{N}_j-1} \hat{s}_{j,m,X}^{(p)}\hat{s}_{j,0,Y}^{(p)} + \frac{1}{2}\sum_{m=-(\widetilde{N}_j-1)}^{\widetilde{N}_j-1} \left[\widehat{C}_{j,0,XY}^{(p)}\right]^2. \qquad (9)$$

The estimator $\widetilde{\mathcal{V}}_j$ is unbiased when $\tau = 0$ [*Whitcher*, 1998]. Under the assumption that the spectral estimates are close to the true values, an approximate $100(1-2p)\%$ confidence interval for $\gamma_{XY}(\lambda_j)$ is

$$\left[\tilde{\gamma}_{XY}(\lambda_j) - \Phi^{-1}(1-p)\sqrt{\frac{\widetilde{\mathcal{V}}_j}{\widetilde{N}_j}} \;,\;\; \tilde{\gamma}_{XY}(\lambda_j) + \Phi^{-1}(1-p)\sqrt{\frac{\widetilde{\mathcal{V}}_j}{\widetilde{N}_j}} \right],$$

where $\Phi^{-1}(p)$ is the $p \times 100\%$ percentage point for the standard normal distribution. Empirical evidence from the wavelet variance suggests that $\widetilde{N}_j = 128$ is a large enough number of wavelet coefficients for such large sample theory to be a good approximation. We adopt this current rule of thumb when constructing approximate CIs for the wavelet covariance.

4.2. Wavelet Cross-correlation

We now use the large sample theory developed in Section 3.4 to construct an approximate CI for the MODWT estimator of the wavelet cross-correlation. Given the non-normality of the correlation coefficient for small sample sizes a nonlinear transformation, Fisher's z-transformation, is sometimes required in order to produce a sample correlation coefficient which is approximately Gaussian distributed and whose shape is independent of the true correlation coefficient [Kotz *et al.* 1982, Volume 3]. Let

$$h(\rho) \equiv \frac{1}{2} \log \left(\frac{1 + \rho}{1 - \rho} \right) = \tanh^{-1}(\rho)$$

define the transformation. For the estimated correlation coefficient $\hat{\rho}$, based on n independent samples, $\sqrt{n-3}(h(\hat{\rho}) - h(\rho))$ has approximately a $N(0,1)$ distribution.

An approximate $100(1 - 2p)\%$ CI for $\rho_{XY}(\lambda_j)$ based on the MODWT is therefore

$$\left[\tanh \left\{ h[\, \tilde{\rho}_{XY}(\lambda_j)] - \frac{\Phi^{-1}(1 - p)}{\sqrt{\widehat{N}_j - 3}} \right\} , \quad \tanh \left\{ h[\, \tilde{\rho}_{XY}(\lambda_j)] + \frac{\Phi^{-1}(1 - p)}{\sqrt{\widehat{N}_j - 3}} \right\} \right]$$

where $\widehat{N}_j = N_j - L'_j$ and $L'_j = \lceil (L - 2)(1 - 2^{-j}) \rceil$ is the number of DWT coefficients associated with scale λ_j. We are using the number of wavelet coefficients as if $\tilde{\rho}_{XY}(\lambda_j)$ had been computed using the DWT because, under the assumptions of Fisher's z-transformation, the denominator should consist of the number of independent samples used in constructing the correlation coefficient. If the autospectra and cross spectrum of the two processes $\{X_t, Y_t\}$ are slowly varying over each octave band of the DWT, the assumption of uncorrelated DWT coefficients is justified; see *McCoy and Walden* [1996] and the references contained therein. This property simply does not hold for the MODWT coefficients because of their lack of downsampling. If an equivalent degrees of freedom argument were available for the wavelet cross-covariance, as was used when establishing CIs for the wavelet variance based on the MODWT [*Percival*, 1995], this could be used instead of $\widehat{N}_j$.

5. Application to Atmospheric Time Series

5.1. Introduction

The relationship between ENSO events and the MJO is a topic that could benefit by using wavelet techniques, which explore the time-varying structure of variability across wavelet scales. To investigate how these two atmospheric phenomena interact, we analyze two time series. The first one is the Southern Oscillation Index (SOI) [*Walker*, 1928], which is an indicator of ENSO. The conventional SOI is defined to be the difference between monthly averages of the station pressure series from climate stations at Darwin, Australia (130.8°E, 12.4°S) and Tahiti, French Polynesia (149°W, 14°S).

We deviate slightly from the usual definition of the SOI by dealing with a daily version of it (this daily version has the same large scale properties as more common definitions of the SOI, but it allows us to explore small scale properties of possible interest). We obtained daily pressure readings from Darwin and Tahiti starting in 1 June 1957 and continuing through 31 December 1992 ($N = 12,998$) and differenced them; see Figure 1 for the individual series. The distance of the stations from the equator is apparent in the strong annual component in each station pressure series. The measurements in the summer and winter of 1983 appear to be lower for the Tahiti station pressure and significantly suppressed for the Darwin station pressure than those in adjacent years. This approximately corresponds to a large ENSO event in the early 1980s.

This daily SOI contains a variety of time-scales associated with atmospheric phenomena. Low frequency fluctuations (interannual time scale) are known to be strongly correlated with ENSO activity. The series probably contains, but is not limited to, energy associated with large-scale westward propagating 6–30 day equatorial Rossby waves [*Krishnamurti and Ardanuy*, 1980; *Kiladis*, 1998], the global 5–day wave [*Madden and Julian*, 1972] and the MJO. We would like to quantitatively analyze the

interannual variability of this series of station pressure differences over a wide range of frequencies; see also *Gambis* [1992].

We also obtained daily station pressure (SP) readings from Truk Island (7.4°N, 151.8°W) as an indicator of the MJO. This series also exists from 1 June 1957 to 31 December 1992; see Figure 1. Unlike the Darwin and Tahiti station pressure series, there is no apparent annual trend given its close proximity to the equator. Missing values in all time series were replaced by one-step-ahead predictions from an ARIMA(3,1,0) model applied to the series [*Jones*, 1980].

5.2. Time-Domain and Spectral Analysis

Here we analyze the SOI and Truk Island SP series using standard time and frequency domain techniques. The cross-correlation sequence is typically estimated by utilizing the biased estimates of the autocovariance sequences for $\{X_t\}$ and $\{Y_t\}$, and their cross-covariance sequence. The estimated cross-correlation sequence for the SOI and Truk Island SP series is shown in Figure 2. The maximum occurs at a lag of +1 days. We also observe the characteristic broad-band peak commonly found in atmospheric time series from this region, with a approximate range of 35–55 day lags.

A bivariate spectral analysis of these data (Figure 3) provides some insight into the possible relationship between ENSO events and the MJO. A Parzen smoothing window was applied to the periodogram with the window parameter chosen such that the spectral window bandwidth was 0.0081 day^{-1}, as in *Madden and Julian* [1971]. The lag window co-spectrum between the SOI and Truk Island SP series exhibits a large peak at the lower frequencies, which include the annual and inter-annual cycles, and two distinct peaks (centered at approximately 36.6 day and 61.3 day periods) in the frequency range of the MJO.

We can test, at the α level of significance, the null hypothesis of zero mean squared coherence (MSC) by checking the estimated MSC, on a frequency by frequency basis,

against $1 - \alpha^{2/(\nu-2)}$ and rejecting if the estimated MSC exceeds it [*Koopmans*, 1974, p. 284]. The parameter ν is the number of equivalent degrees of freedom associated with the spectral estimates; $\nu \approx 189$ using Table 269 in *Percival and Walden* [1993]. We see that both peaks are significant at the 5% and 1% levels for a broad range of frequencies. This agrees with previous studies on the large-scale structure of the MJO; see, e.g., *Kiladis and Weickmann* [1992], *Hendon and Salby* [1994] and *Bantzer and Wallace* [1996].

5.3. Wavelet Analysis of Variance/Covariance

Daily measurements allow us to apply the MODWT and analyze the wavelet sub-series which correspond to band-pass filtered series with approximate pass-band $1/2^{j+1} \leq |f| \leq 1/2^j$. Although a large annual cycle is observed in the daily SOI series, it is unnecessary to remove any semi-annual components due to the approximate band-pass nature of the MODWT which should be roughly captured in wavelet scale λ_7 (128–256 day periods) or annual components which should be captured in the wavelet scale λ_8 (256–512 day periods). To investigate this, we looked at the product of the squared gain function of the LA(8) wavelet filter – the Daubechies compactly supported least asymmetric wavelet filter with eight non-zero coefficients – and the periodogram of the Truk Island SP series and daily SOI (not shown). No significant influence was found by the annual cycle for the Truk Island SP series. Several frequencies corresponding to the annual cycle are prominent in wavelet scale λ_8 (which captures 256–512 day periods) and also in wavelet scale λ_7 (periods of 128–256 days) where it accounts for approximately 27% of the variance. Wavelet scales λ_6 and λ_9 (64–128 and 512–1024 day periods) are only slightly affected by the annual cycle where it accounts for less than 1% and 6% of the variance, respectively. The semi-annual cycle exerts even less influence over its adjacent wavelet scales. A similar argument was made when band-pass filtering atmospheric time series in Anderson *et al.* [1984] for MJO time scales. The MJO is

known to occur with periods of around 30–60 days. We therefore expect to see it in wavelet scale λ_5 – associated with changes of 16 days, an approximate pass-band of $1/64 \leq |f| \leq 1/32$ and 32–64 day periods.

A partial MODWT ($J = 10$) was applied to each series using the Daubechies least asymmetric wavelet filter of length $L = 8$ – which we denote by LA(8). Figures 4 and 5 give the MODWT coefficients for the Truk Island SP series and daily SOI, respectively. Each wavelet and scaling coefficient vector has been circularly shifted in order to obtain an approximate zero-phase filter, allowing us to align features across scales; see *Percival and Mofjeld* [1997] for more details. For the Truk Island SP series, we observe only a slight annual trend in the $\widetilde{\mathbf{W}}_8$ series and the large disruption in the early 1980s appears to primarily affect wavelet scales λ_7 through λ_{10} (128–2048 day periods). The $\widetilde{\mathbf{W}}_5$ series, associated with periods in the range of the MJO, appears to fade in-and-out in amplitude with no apparent pattern. The daily SOI wavelet decomposition exhibits a strong annual trend where the disturbance in the early 1980s affects the wavelet scales λ_8 through λ_{10} (256–2048 day periods). Again, the wavelet scale λ_5 – associated with the MJO – exhibits numerous bursts over the length of the time series.

If we are to investigate a possible lead/lag relationship between the two series, then the wavelet cross-correlation must be estimated for various lags. Figure 6 shows the estimated wavelet cross-correlation between the daily SOI and Truk Island SP series. Different ranges of lags were used depending on the period of oscillations captured by the wavelet coefficients – with the first three wavelet scales displayed on lags ± 60, wavelet scales λ_4 through λ_6 on lags ± 120 and wavelet scales λ_7 through λ_{10} on lags ± 240. Lower wavelet scales do not exhibit cross-correlations significantly different from zero for larger lags. Confidence intervals (dotted lines) were computed from Section 4.2. The large positive peak in the first five vectors of wavelet coefficients is at a lag of 1 day for wavelet scales λ_1 and λ_2 (2–4 day and 4–8 day periods, respectively), a lag of 2 days for wavelet scale λ_3 (8–16 day periods), a lag of 4 days for wavelet scale λ_4 (16–32 day

periods) and zero days for wavelet scale λ_5 (32–64 day periods).

There is an obvious asymmetry in the wavelet cross-correlation for wavelet scales λ_4 and higher (periods of 16 days and longer). The analysis here was performed so that at a lag of +1 day, the daily SOI time series leads the Truk SP series. As already noted for wavelet scale λ_5 (32–64 day periods), the largest positive cross-correlation occurs at lag zero. The largest negative cross-correlation is at a lag of 20 days, approximately half the period of the MJO, and the second largest positive cross-correlation occurs at a lag of 41 days, approximately a full period of the MJO. Even though the daily SOI consists of a difference between two stations with different spatial locations, there is still a strong 40 day oscillation which is correlated (and in phase) with the Truk Island SP series. It is also interesting to note that the wavelet cross-correlation for the first three wavelet scales is essentially an odd function. In contrast, the wavelet cross-correlation for wavelet scales λ_6 (64–128 day periods) and λ_7 (128–256 day periods) are essentially even functions. Patterns in higher scales (lower frequencies) correspond to the annual and inter-annual trends.

Although direct comparison between Figure 6 and Figure 2 is not appropriate, because the wavelet correlation does not decompose the correlation between two stationary processes, the wavelet covariance does decompose the covariance between two time series. Since the wavelet correlation is simply the wavelet covariance standardized at each scale, the shape of each wavelet cross-correlation is the same even though the magnitudes are off. Hence, we may make a rough comparison between the two, keeping in mind the facts just stated.

The first obvious difference is the fact that usual cross-correlation is positive for all negative lags. Looking at Figure 6, we see that the wavelet cross-correlation for scales λ_9 (512–1024 day periods) and λ_{10} (1024–2048 day periods) are all positive and contribute to this feature, whereas for positive lags they are close to zero and allow the wavelet scale λ_8 (256–512 day periods), which captures the annual frequency, to dominate.

The two dips on either side of the peak at a lag of +1 days is the superposition of the first six scales in Figure 6. The subsequent peak around a lag of +40 days is a result of the anti-correlation for wavelet scales λ_5 (32–64 day periods) and λ_6 (64–128 day periods) reducing the annual cross-correlation component (wavelet scale λ_8) for smaller lags. This leads to a different interpretation than what is seen by looking at the usual cross-correlation sequence. The correlation structure, when applied to all scales simultaneously, results in a quite complex looking cross-correlation sequence. When broken up with the wavelet transform a few simple, yet distinct, patterns appear which may be associated with known atmospheric phenomena.

5.4. Investigating Seasonal Variation in the Madden–Julian Oscillation

Up to this point in the analysis, we have largely ignored an important feature of the DWT, its ability to extract information which is local in time. With respect to these data, the question of whether or not the MJO changes over time is of particular interest. Variations in the data could have (at least) two potential meanings: that the strength of the MJO is changing over time or that the frequency of the MJO is changing over time. The first type of change would produce a pattern of increasing and decreasing coefficients for the time-varying wavelet variance; i.e., the squared wavelet coefficients at the same scale (recall that the MJO should be captured in the wavelet scale λ_5 coefficients – associated with 32–64 day periods). The second type of change would not only produce differing magnitudes of the time-varying wavelet variance, but, if the change in frequency was large enough, a shift of large coefficients from one scale to another. *Madden and Julian* [1994] investigated the latter type of change, with respect to the MJO at Truk Island, using univariate spectral methods.

Let us investigate the possibility of a changing MJO over time by computing the time-dependent wavelet variance $\nu_t^2(\lambda_j)$, where t denotes time in days, for the Truk Island SP series and daily SOI individually. Averaging over all time-dependent wavelet

variances within each season, we may obtain seasonal wavelet variances for both series; denoted as $\tilde{\nu}_s^2(\lambda_j)$ where $s \in \{summer, winter\}$. Figure 7 shows the seasonal wavelet variance for the daily SOI and Truk Island SP series. Approximate confidence intervals were computed using the conservative formula η_3 for the equivalent degrees of freedom as given in *Percival* [1995]. The Truk Island SP series exhibits increased wavelet variance in the winter (defined to be November–April) across wavelet scales λ_4 to λ_7 (periods of 16–256 days). The daily SOI also exhibits increased wavelet variance in the winter across wavelet scales λ_4 to λ_6 (Fourier periods of 16–128 days).

Figure 8 shows the estimated seasonal wavelet correlation $\tilde{\rho}_s(\lambda_j)$ between the daily SOI and Truk Island SP series at a lag of zero days. The seasonal wavelet correlation appears to be significantly different from zero (in fact, positive) for all wavelet scales except λ_7 (128–256 day periods) during the winter. In the summer, the seasonal wavelet correlation is positive for small wavelet scales λ_1 to λ_3 (2–16 day periods), slightly negative for the wavelet scale λ_4 (16–32 day periods), not significantly different from zero for wavelet scales λ_5 to λ_7 (32–256 day periods) and positive for all periods longer than 256 days. When comparing summer and winter seasonal wavelet correlations, they are significantly different for wavelet scales λ_4 to λ_6 – corresponding to periods of 16–128 days. Restricting ourselves to less than the annual periods, the winter wavelet correlation is strongest within 32–64 day oscillations with a value of $\tilde{\rho}_{winter}(\lambda_5) = 0.38$ and approximate 95% CI $[0.30, 0.46]$.

Figure 9 gives the estimated seasonal wavelet cross-correlation $\tilde{\rho}_{\tau,s}(\lambda_j)$ between the Truk Island SP series and the daily SOI with approximate 95% CIs given by the dotted lines. To compute $\tilde{\rho}_{\tau,s}(\lambda_j)$, the seasonal wavelet cross-correlations for each individual year were treated as independent and averaged together. The number of displayed lags is as in Figure 6. The summer and winter wavelet cross-correlation sequences are almost identical for periods of 2–8 days and differ only slightly for 8–16 day periods. A striking feature is seen for longer period wavelet scales where $\tilde{\rho}_{\tau,winter}(\lambda_4)$, $\tilde{\rho}_{\tau,winter}(\lambda_5)$ and

$\tilde{\rho}_{\tau,winter}(\lambda_6)$ show a strong pattern of the daily SOI leading the Truk Island SP series. While this is not as apparent in $\tilde{\rho}_{\tau,summer}(\lambda_4)$ and $\tilde{\rho}_{\tau,summer}(\lambda_5)$, it is a complete reversal of the pattern for $\tilde{\rho}_{\tau,summer}(\lambda_6)$ where the Truk Island SP series leads the daily SOI!

When the time-dependent wavelet variance was plotted (not shown here), the most extreme years for the winter wavelet variance $\tilde{\nu}^2_{winter}(\lambda_5)$ – periods of 32–64 days – appeared to be 1961, 1986 and 1992 for the daily SOI and for the Truk Island SP series, 1959, 1974, 1978 and 1990. These extreme years for the Truk Island SP series before 1990 agree with results from Anderson *et al.* [1984].

It is evident, from the analysis presented here, that a seasonal pattern exists in the Madden–Julian oscillation – even in locations close to the equator [*Madden,* 1986; *Anyamba and Weare,* 1995]. Although multiscale patterns in the SOI were identified by *Gambis* [1992] through use of the CWT, we provide the ability to perform hypothesis tests between estimated variances and correlations associated with specific physical time scales.

5.5. Investigating ENSO Variation of the Madden–Julian Oscillation

We have already seen how the association between the daily SOI and SP series collected at Truk Island, for wavelet scales associated with the MJO, exhibits different characteristics between summer and winter seasons. Now we propose to quantitatively analyze the same association between different episodes of ENSO activity.

The conventional SOI, computed via monthly differences between Tahiti and Darwin, is a measure of the strength of the trade winds, where high SOI (pressure difference from East to West) is associated with La Niña conditions and low SOI (pressure difference from West to East) is associated with El Niño conditions. To construct a useful indicator of ENSO activity from the data presented here, the wavelet smooth ($\widetilde{\mathcal{S}}_8$) from a multiresolution analysis ($J = 8$) of the daily SOI was extracted; see *Percival and Mofjeld* [1997] for more details on a MODWT multiresolution analysis.

This series represent all periods greater than 512 days. The sample mean was removed and the series was then inverted in order to agree with the conventional SOI taken from the NCEP-CPC website[1]; see Figure 10. Let us define this 'low frequency' wavelet-based indicator of ENSO activity via $\text{SOI}_{LF} \equiv -\widetilde{\mathcal{S}}_8 + \overline{\widetilde{\mathcal{S}}_8}$, where $\overline{X}$ is the sample mean. There is excellent agreement between the SOI_{LF} and the conventional SOI, our wavelet-based indicator being much smoother. We see the large El Niño events of 1981–1982 and 1986–1987, with a subsequent La Niña event in 1988–1989.

Another measure of ENSO activity is available from a subjective classification procedure using reanalyzed sea surface temperatures produced at NCEP-CPC and UKMO, provided on a quarterly time scale. These data are also available from the NOAA-CPC website[2]. The points agree with the large deviations of the SOI_{LF}, but disagree when the deviations are moderate; e.g., 1962, 1967–1968, 1981 and 1984–1985.

Kiladis and Diaz [1989] provides a list of year 0s for warm and cold events, over the period 1877–1988, based on the conventional SOI and an SST anomaly index for the eastern equatorial Pacific. Year 0 of a warm event is defined to be the year in which the SOI changes sign from positive to negative and eastern equatorial Pacific SST anomalies become strongly positive. For the period coinciding with this study (1957–1988), warm events were found to begin in 1957, 1963, 1965, 1969, 1972, 1976, 1982 and 1986. These events agree with the SOI_{LF}, which is based solely on the low-frequency content of daily station pressure differences between Darwin and Tahiti. Cold events were documented to start in 1964, 1970, 1973, 1975 and 1988. The cold events do not agree exactly with the SOI_{LF}, but do agree very well with the subjective classification from NCEP-CPC and UKMO.

Figure 11 gives the wavelet variance for the Truk Island SP series partitioned into

---

[1]ftp://ftp.ncep.noaa.gov/pub/cpc/wd52dg/data/indices/soi

[2]http://www.cpc.ncep.noaa.gov/products/analysis_monitoring/ensostuff/ensoyears.html

warm, cold, and other (not warm nor cold) episodes. The top plots uses the classification from NCEP-CPC while the bottom plots uses the SOI_{LF} (Figure 10). A threshold of ± 0.5 was used to define the three episodes; i.e.,

$$
\begin{aligned}
\widetilde{\mathcal{S}}_{8,t} &< -0.5 &\implies& \quad \text{warm event day;} \\
-0.5 \leq \widetilde{\mathcal{S}}_{8,t} &\leq 0.5 &\implies& \quad \text{``other'' day;} \\
\widetilde{\mathcal{S}}_{8,t} &> 0.5 &\implies& \quad \text{cold event day.}
\end{aligned}
\tag{10}
$$

The general shape of each plot (top and bottom) is quite similar, but the relation between warm, cold and other wavelet variances differs substantially. Under the NCEP-CPC classification, the wavelet variance for warm episodes is significantly greater than cold events only in the first three wavelet scales (2-16 day periods). Under the wavelet-based classification, the wavelet variance for warm episodes is significantly less than both cold and other episodes for wavelet scales λ_4 and λ_5 (16–64 day periods). The "warm" wavelet variance inverts this property, becoming greater than the wavelet variances for cold and other episodes for periods greater than 128 days (although only significantly for 128–256 day periods).

The wavelet variance for the daily SOI, partitioned into warm, cold, and other episodes, is given in Figure 12. As was observed with the Truk Island SP series, the general shape of the wavelet variance across scales does not vary drastically whether using the NCEP-CPC or the wavelet-based classification (Equation (10)). We observe the wavelet variance for cold episodes to be less than either the warm or other episodes for wavelet scales λ_3 to λ_6 (8–128 day periods), although only significantly different for periods of 16–64 days, under the NCEP-CPC classification. The "cold" wavelet variance then is greater than the wavelet variance for warm episodes for wavelet scales λ_7 and λ_8 (128–512 day periods). These comparisons are similar under the wavelet-based classification of episodes, but do not appear to be statistically significant.

Figure 13 provides the wavelet correlation between daily SOI and the Truk Island SP series under different episodes of ENSO activity. We will concentrate on comparisons

under the wavelet-based classification of ENSO activity given by Equation (10); bottom plot of Figure 13. For a large range of wavelet scales, the wavelet correlation between these two series is not significantly different from zero for warm ENSO episodes (Fourier periods of 8–32 days and 64–512 days). Even under wavelet scale λ_5 (32–64 day periods), which should capture the MJO, the "warm" wavelet correlation $\tilde{\rho}_{warm}(\lambda_5) = 0.12$ with an approximate 95% CI of $[0.02, 0.21]$. This agrees with previous studies which indicate the suppression of the MJO during El Niño events [Anyamba and Weare 1995; Hendon *et al.* 1999]. We also note the rather large correlation between the daily SOI and Truk Island SP series for 256–512 day periods under cold episodes ($\tilde{\rho}_{cold}(\lambda_8) = 0.76$ with an approximate 95% CI of $[0.62, 0.86]$) while under warm episodes the wavelet correlation is almost zero ($\tilde{\rho}_{warm}(\lambda_8) = 0.03$ with an approximate 95% CI of $[-0.26, 0.30]$).

The wavelet cross-correlation between the daily SOI and Truk Island SP series, partitioned into warm, cold, and other episodes, is given in Figure 14. The first two wavelet scales (corresponding to 2–4 and 4–8 day periods) are very similar in pattern between the three ENSO episodes, only slightly increased in magnitude during La Niña (cold) events. For larger wavelet scales, all three episodes (warm, cold and other) differ from each other in shape and magnitude. When comparing these wavelet cross-correlation sequences associated with ENSO episodes to the global wavelet cross-correlation in Figure 6, the periods marked as "other" are most similar to the global estimates. When comparing $\tilde{\rho}_{\tau,e}(\lambda_4)$ for $e \in \{cold, warm, other\}$, the cold and other wavelet cross-correlations are similar around lag zero, while the warm wavelet cross-correlation looks nothing like the other two (exhibiting its largest coefficient around $\tau = 80$). While $\tilde{\rho}_{\tau,other}(\lambda_5)$ exhibits the usual pattern with a large positive correlation at $\tau = 0$ and a large negative correlation around $\tau = 20$, $\tilde{\rho}_{\tau,cold}(\lambda_5)$ exhibits a very small negative correlation at $\tau = 20$ and $\tilde{\rho}_{\tau,warm}(\lambda_5)$ is reduced in magnitude and translated to the left. The wavelet cross-correlations for scale λ_6 show a variety of patterns, again with $\tilde{\rho}_{\tau,other}(\lambda_6)$ matching closely to the global wavelet cross-correlation

in Figure 6.

6. Summary and Conclusions

We have introduced a new analysis technique for bivariate Gaussian time series which utilizes a non-decimated version of the DWT – the maximal overlap DWT. Both stationary and certain non-stationary processes are easily handled by this methodology. As is the case with the wavelet variance, natural estimators of the covariance and correlation between two time series are defined as alternatives to the Fourier-based cross spectrum and magnitude squared coherence. The wavelet covariance and wavelet correlation are generalized to the wavelet cross-covariance and wavelet cross-correlation, respectively, which also decompose their classical counterparts on a scale by scale basis. Thus, complicated patterns of association between time series are broken down into several much simpler patterns – each one associated with a physical time scale. With any good statistical analysis a measure of variability is also required. We provide approximate confidence intervals for our wavelet estimators and therefore allow for straightforward statistical hypothesis testing.

A major advantage to wavelet techniques is their ability to decompose a time series locally both in frequency and time. We utilize this property to investigate behavior of the MJO with respect to seasons (boreal summer and winter) and also ENSO activity (El Niño, La Niña and other periods). We find significantly higher variability during boreal winter in both the Truk Island SP series and SOI for periods corresponding to with MJO, agreeing with the qualitative results of *Gambis* [1992], and suppression of variability during boreal summer, agreeing with *Madden* [1986] and *Anyamba and Weare* [1995]. Correlation between the Truk Island SP series and daily SOI for periods of 32–64 days was found to be quite strong and significantly different from zero in boreal winter, while it was not significantly different from zero in boreal summer and cross-correlations between the two series are also stronger in the boreal winter. *Gutzler*

[1991] found increased climatological variance in the boreal summer versus winter of band-pass filtered anomalies (31–66 day periods) of surface zonal winds at Truk Island, and negative correlations in boreal summer between interannual variations of the SOI and band-pass filtered anomalies of surface zonal winds. Similar statements to the ones in this paper are not available from *Gutzler* [1991] since measures of variability in the estimates (e.g., approximate confidence intervals) were not provided.

After classifying our time series into El Niño and La Niña events, we found significantly lower variance in the 32–64 day filtered Truk Island SP series during El Niño events which agrees with Hendon *et al.* [1999] where MJO activity was noted to diminish during exceptional warm events. *Gutzler* [1991] found no correlation between seasonally averaged 31–66 day band-pass filtered variance in the upper troposphere and the SOI. The wavelet correlations we found for all events are significantly different from zero, but they are not significantly different from each other. This disagrees with the finding that the ratio of the observed points belonging to El Niño events to the number of high-frequency events was higher than expected by chance as discussed in *Gambis* [1992]. Even though the correlations are not significantly different between ENSO periods, the interesting feature here is that the wavelet cross-correlations for specific Fourier periods do exhibit marked change in their structure. Figure 14 shows an almost symmetric lead/lag relation between the Truk Island SP series and daily SOI measurements for 32–64 day periods during La Niña events whereas the daily SOI leads the SP series with a large negative correlation at a positive lag around half the period of the MJO is apparent in El Niño and other periods. Higher frequency events, such as those associated with changes spanning 2–8 days, are very similar between El Niño and La Niña events, with only a slight increase in magnitude of correlations during La Niña events.

Although the time series used here only capture large spatial-scale features of the MJO and SOI, still several interesting features were observed and statistically tested

through our methodology. The application provided here hopefully gives a indication of the potential use of wavelet estimators in the atmospheric sciences.

References

Anderson, J. R., D. E. Stevens, and P. R. Julian (1984). Temporal variations of the tropical 40–50 day oscillation. *Monthly Weather Review 112*(12), 2431–2438.

Anyamba, E. K. and B. C. Weare (1995). Temporal variability of the 40–50-day oscillation in tropical convection. *International Journal of Climatology 15*(4), 379–402.

Bantzer, C. H. and J. M. Wallace (1996). Intraseasonal variability in tropical mean temperature and precipitation and their relation to the tropical 40–50 day oscillation. *Journal of the Atmospheric Sciences 53*(21), 3032–3045.

Brillinger, D. R. (1979). Confidence intervals for the crosscovariance function. In *Mathematical Statistics*, Volume 5 of *Selecta Statistica Canadiana*, pp. 1–16. Hamilton, Ontario: McMaster University Printing Services.

Daubechies, I. (1992). *Ten Lectures on Wavelets*, Volume 61 of *CBMS-NSF Regional Conference Series in Applied Mathematics*. Philadelphia: Society for Industrial and Applied Mathematics.

Foufoula-Georgiou, E. and P. Kumar (Eds.) (1994). *Wavelets in Geophysics*, Volume 4 of *Wavelet Analysis and its Applications*. San Diego: Academic Press, Inc.

Gambis, D. (1992). Wavelet transform analysis of the length of the day and El-Niño/Southern Oscillation variations at intraseasonal and interannual time scales. *Annales Geophysicae 10*, 429–437.

Gray, B. M. (1988). Seasonal frequency variations of the 40–50 day oscillation. *Journal of Climatology 8*, 511–519.

Gutzler, D. S. (1991). Interannual fluctuations of intraseasonal variance of near-equatorial zonal winds. *Journal of Geophysical Research 96 (D Suppl.)*, 3173–3185.

Hendon, H. H. and M. L. Salby (1994). The life cycle of the Madden–Julian oscillation. *Journal of the Atmospheric Sciences 51*, 2225–2237.

Hendon, H. H., C. Zhang, and J. D. Glick (1999). Interannual variation of the Madden–Julian oscillation during austral summer. *Journal of Climate 12*, 2538–2550.

Hudgins, L., C. A. Friehe, and M. E. Mayer (1993). Wavelet transforms and atmospheric turbulence. *Physical Review Letters 71*(20), 3279–3282.

Hudgins, L. H. (1992). *Wavelet Analysis of Atmospheric Turbulence*. Ph. D. thesis, University of California, Irvine.

Jones, R. H. (1980). Maximum likelihood fitting of ARMA models to time series with missing observations. *Technometrics 22*(3), 389–395.

Kestin, T. S., D. J. Karoly, J. I. Yano, and N. A. Rayner (1998). Time-frequency variability of ENSO and stochastic simulations. *Journal of Climate 11*(9), 2258–2272.

Kiladis, C. N. (1998). Observations of Rossby waves linked to convection over the eastern tropical Pacific. *Journal of the Atmospheric Sciences 55*(3), 321–339.

Kiladis, C. N. and K. M. Weickmann (1992). Extratropical forcing of tropical Pacific convection during northern winter. *Monthly Weather Review 120*(9), 1924–1938.

Kiladis, G. N. and H. F. Diaz (1989). Global climatic anomalies associated with extremes in the Southern Oscillation. *Journal of Climate 2*, 1069–1090.

Koopmans, L. H. (1974). *The Spectral Analysis of Time Series*. New York. Academic Press.

Kotz, S., N. L. Johnson, and C. B. Read (Eds.) (1982). *Encyclopedia of Statistical Sciences*. New York: Wiley.

Krishnamurti, T. N. and P. A. Ardanuy (1980). The 10 to 20–day westward propagating mode and "breaks in the monsoons". *Tellus 32*, 15–26.

Kuhnel, I. (1989). Spatial and temporal variations in Australo–Indonesian region cloudiness. *International Journal of Climatology 9*(4), 395–405.

Kumar, P. (1996). Role of coherent structures in the stochastic-dynamic variability of precipitation. *Journal of Geophysical Research-Atmospheres 101*(D21), 26,393–26,404.

Kumar, P. and E. Foufoula-Georgiou (1994). Wavelet analysis in geophysics: An introduction. See *Foufoula-Georgiou and Kumar* [1994], pp. 1–43.

Lindsay, R. W., D. B. Percival, and D. A. Rothrock (1996). The discrete wavelet transform and the scale analysis of the surface properties of sea ice. *IEEE Transactions on Geoscience and Remote Sensing 34*(3), 771–787.

Liu, P. C. (1994). Wavelet spectrum analysis and ocean wind waves. See *Foufoula-Georgiou and Kumar* [1994], pp. 151–166.

Madden, R. A. (1986). Seasonal variation of the 40–50 day oscillation in the tropics. *Journal of the Atmospheric Sciences 43*(24), 3138–3158.

Madden, R. A. and P. R. Julian (1971). Detection of a 40–50 day oscillation in the zonal wind in the tropical pacific. *Journal of the Atmospheric Sciences 28*, 702–708.

Madden, R. A. and P. R. Julian (1972). Further evidence of global-scale 5-day pressure waves. *Journal of the Atmospheric Sciences 29*, 1464–1469.

Madden, R. A. and P. R. Julian (1994). Observations of the 40–50 day tropical oscillation: A review. *Monthly Weather Review 122*(5), 814–837.

McCoy, E. J. and A. T. Walden (1996). Wavelet analysis and synthesis of stationary long-memory processes. *Journal of Computational and Graphical Statistics 5*(1),

26–56.

Murakami, T. and W. L. Sumathipala (1989). Westerly bursts during the 1982/83 ENSO. *Journal of Climate 2*, 71–85.

Percival, D. B. (1995). On estimation of the wavelet variance. *Biometrika 82*(3), 619–631.

Percival, D. B. and P. Guttorp (1994). Long-memory processes, the Allan variance and wavelets. See *Foufoula-Georgiou and Kumar* [1994], pp. 325–344.

Percival, D. B. and H. O. Mofjeld (1997). Analysis of subtidal coastal sea level fluctuations using wavelets. *Journal of the American Statistical Association 92*(439), 868–880.

Percival, D. B. and A. T. Walden (1993). *Spectral Analysis for Physical Applications: Multitaper and Conventional Univariate Techniques*. Cambridge: Cambridge University Press.

Percival, D. B. and A. T. Walden (2000). *Wavelet Methods for Time Series Analysis*. Cambridge: Cambridge University Press. Forthcoming.

Salby, M. L. and H. H. Hendon (1994). Intraseasonal behavior of clouds, temperature, and motion in the tropics. *Journal of the Atmospheric Sciences 51*(15), 2207–2224.

Torrence, C. and G. P. Compo (1998). A practical guide to wavelet analysis. *Bulletin of the American Meteorological Society 79*(1), 61–78.

Walker, G. T. (1928). World weather. *Monthly Weather Review 56*, 167–170.

Weickmann, K. M. (1991). El Niño/Southern Oscillation and Madden-Julian (30–60 day) oscillations during 1981–1982. *Journal of Geophysical Research 96 (D Suppl.)*, 3187–3195.

Whitcher, B. (1998). *Assessing Nonstationary Time Series Using Wavelets*. Ph. D. thesis, University of Washington.

Whitcher, B., P. Guttorp, and D. B. Percival (1999). Mathematical background for wavelet estimators for cross-covariance and cross-correlation. Technical Report 38, National Research Center for Statistics and the Environment.

7. List of Figures

1. Station pressure series for Truk Island (7.4°N, 151.8°W); Darwin, Australia (12.4°S, 130.9°E); and Tahiti, French Polynesia (17.5°S, 149.5°W). The "staggered" look of the Truk Island series prior to 1971 is the result of rounding to the nearest millibar.

2. Estimated cross-correlation sequence (ccs) for the daily SOI and Truk Island SP series for lags up to ±240 days. The dotted lines represent asymptotic 95% confidence intervals for the ccs.

3. Estimated lag window co-spectrum and magnitude squared coherence (msc) between the daily SOI and Truk Island SP series. A Parzen lag window, with spectral window bandwidth 0.0081 day^{-1}, was applied to the periodogram. The dotted and dashed lines correspond to the 5% and 1% levels of significance test for non-zero msc, respectively.

4. MODWT coefficients for the Truk Island SP series using the LA(8) wavelet filter. The wavelet coefficient vectors $\widetilde{\mathbf{W}}_1, \widetilde{\mathbf{W}}_2, \ldots, \widetilde{\mathbf{W}}_{10}$ are associated with variations on scales of $1, 2, \ldots, 1024$ days and the scaling coefficient vector $\widetilde{\mathbf{V}}_{10}$ is associated with variations of 2048 days or longer.

5. MODWT coefficients for the daily SOI using the LA(8) wavelet filter. The wavelet and scaling coefficients have the same interpretation as in Figure 4.

6. Wavelet cross-correlation between the daily SOI and Truk Island SP series for the first 10 wavelet scales. Approximate 95% confidence intervals (dotted lines) were computed from Section 4.2. The range of lags is ±60 for wavelet scales $\lambda_1, \ldots, \lambda_3$, ±120 for scales $\lambda_4, \ldots, \lambda_6$ and ±240 for scales $\lambda_7, \ldots, \lambda_{10}$.

7. Seasonal wavelet variance for the Truk Island SP series and daily SOI, partitioned

into "summer" (May–October) and "winter" (November–April). Periods (in days) are displayed on the upper axis.

8. Seasonal wavelet correlation between the Truk Island SP series (top plot) and daily SOI (bottom plot), partitioned into "summer" (May–October) and "winter" (November–April). Periods (in days) are displayed on the upper axis.

9. Seasonal wavelet cross-correlation between the Truk Island SP series and daily SOI. The left column of plots gives the "summer" (May–October) values while the right column gives the "winter" (November–April) values for the first six wavelet scales, corresponding to – from bottom to top – periods of 1–2 days, 2–4 days, 4–8 days, 8–16 days, 16–32 days and 32–64 days. The x-axis covers ±60 days for the first (bottom) three wavelet scales and ±120 days for the last (top) three wavelet scales.

10. Wavelet-based indicator of ENSO activity. The solid line in both plots was computed by extracting the wavelet smooth ($\widetilde{\mathcal{S}}_8$) from the MODWT multiresolution analysis ($J = 8$) of the daily SOI. The dotted line in the top plot is the conventional SOI from the NOAA-CPC website. The points in the bottom plot indicate cold (La Niña) and warm (El Niño) events, denoted by $+1$ and -1 respectively. The data comes from a subjective classification procedure using reanalyzed sea surface temperatures produced at NCEP-CPC and UKMO (also available from the NOAA-CPC website).

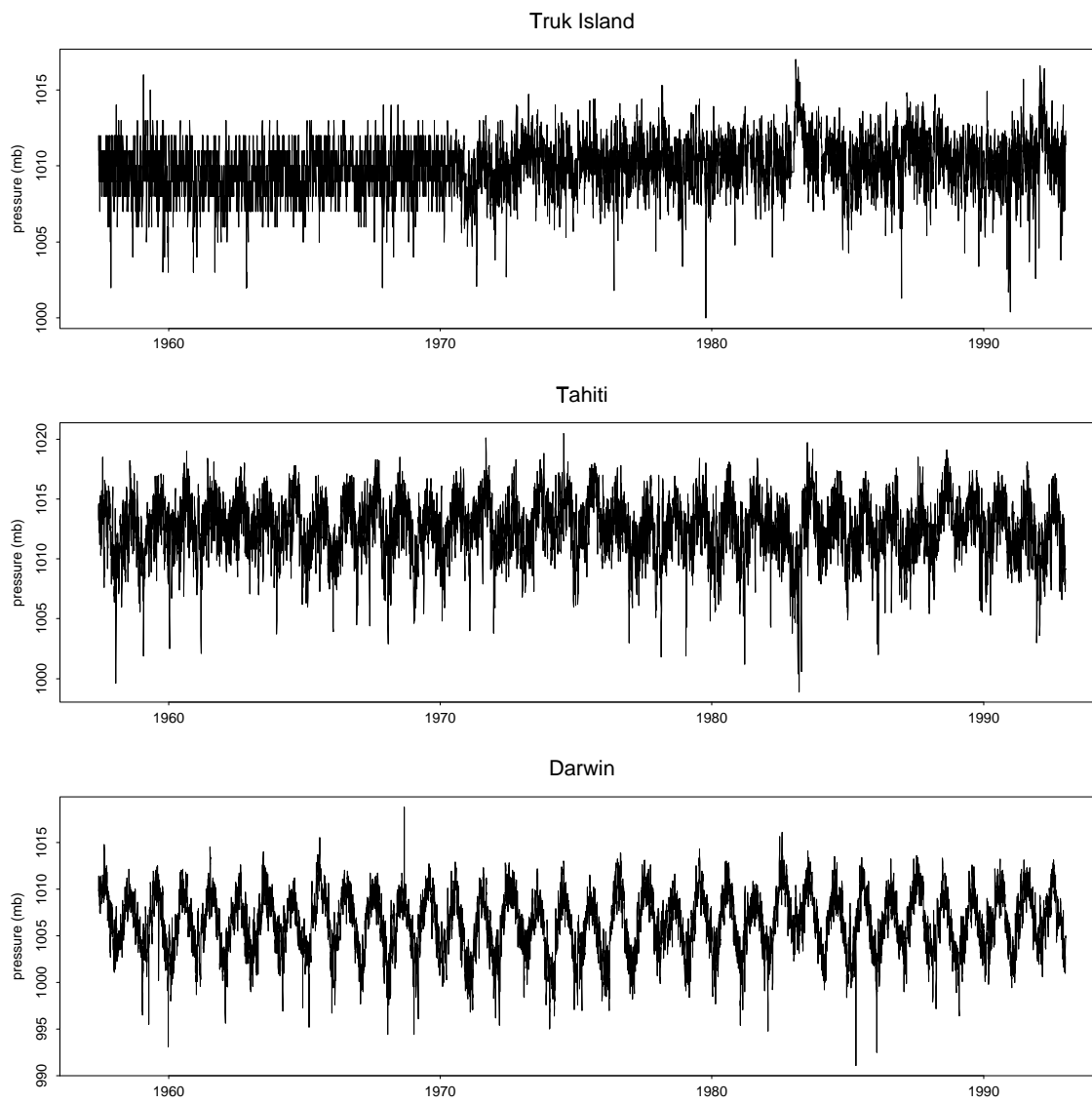11. Wavelet variance for the Truk Island SP series, partitioned into El Niño (warm), La Niña (cold) and "other" episodes. Classifications were made according to the NCEP-CPC definitions of these events (top plot) and wavelet-based ENSO indicator (bottom plot); cf. Figure 10. Periods (in days) are displayed on the upper axis.

12. Wavelet variance for the daily Southern Oscillation Index, partitioned into El Niño (warm), La Niña (cold) and "other" episodes. Classifications were made according to the NCEP-CPC definitions of these events (top plot) and SOI_{LF} (bottom plot); cf. Figure 10. Periods (in days) are displayed on the upper axis.

13. Wavelet correlation between the Truk Island SP series and daily SOI, partitioned into El Niño (warm), La Niña (cold) and "other" episodes. Classifications were made according to the NCEP-CPC definitions of these events (top plot) and the SOI_{LF} (bottom plot); cf. Figure 10. Periods (in days) are displayed on the upper axis.

14. Wavelet cross-correlation between the Truk Island SP series and daily SOI, partitioned into El Niño (warm), La Niña (cold) and "other" episodes. Classifications were made according to the SOI_{LF}; cf. Figure 10.

Figure 1.

Figure 2.

Figure 3.

W1

W2

W3

W4

W5

W6

W7

W8

W9

W10

V10

1960   1970   1980   1990

time (years)

Figure 4.

W1
W2
W3
W4
W5
W6
W7
W8
W9
W10
V10

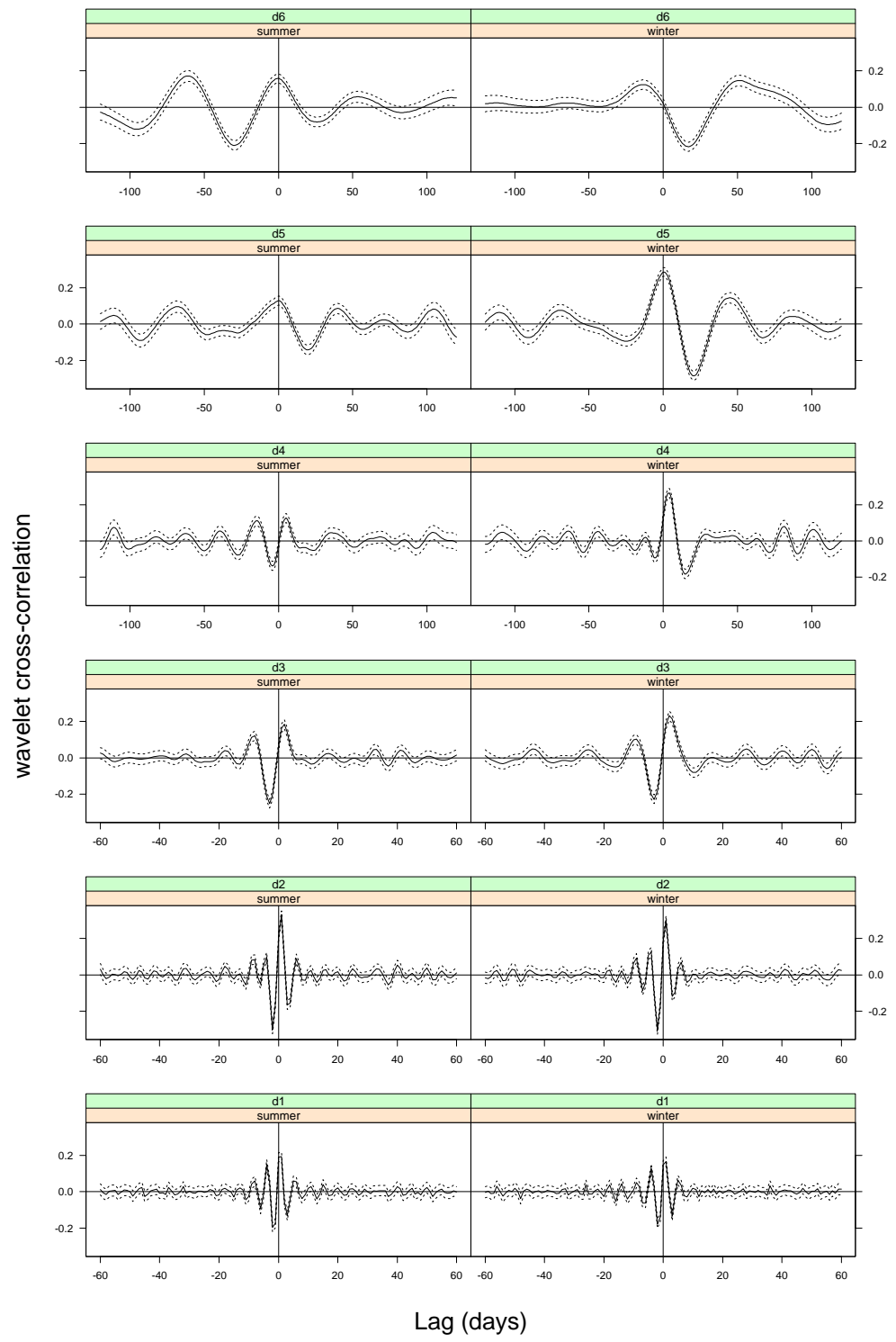1960   1970   1980   1990
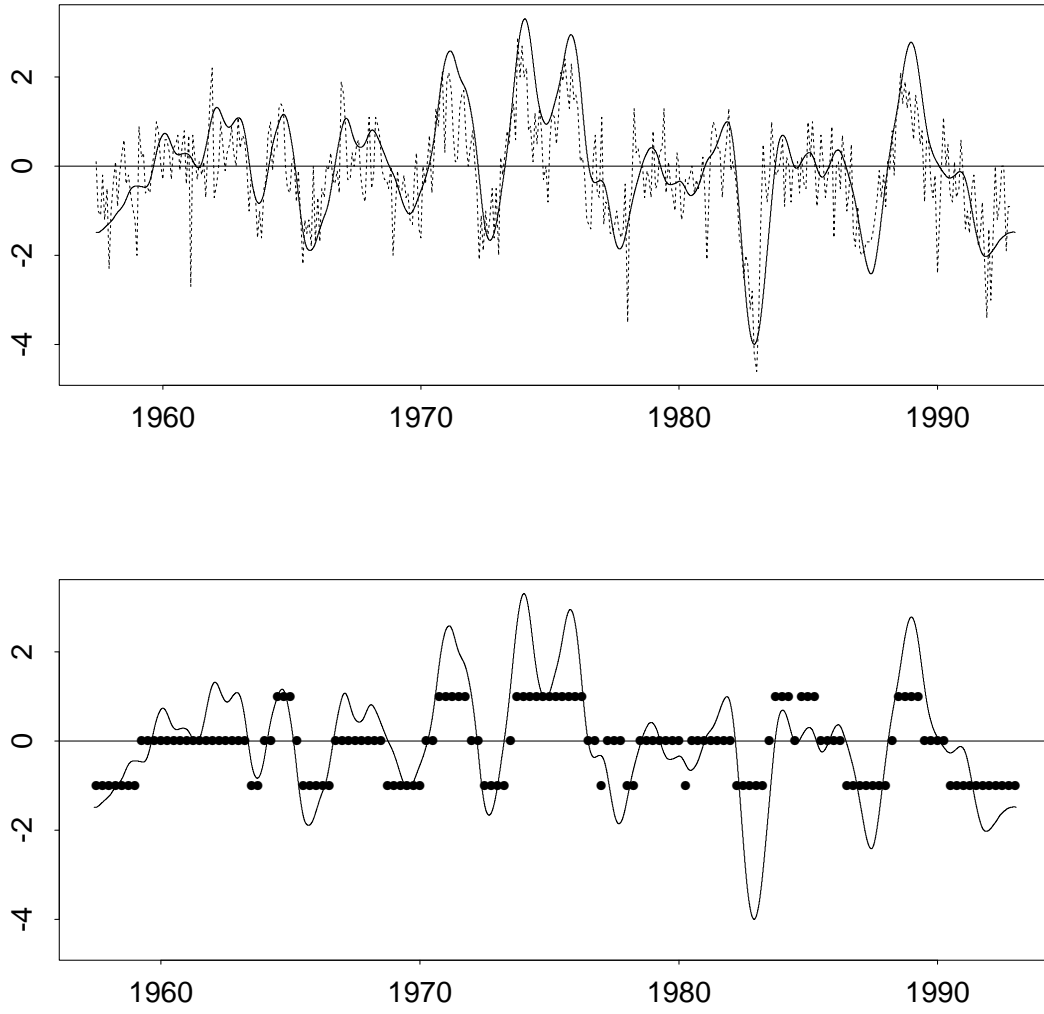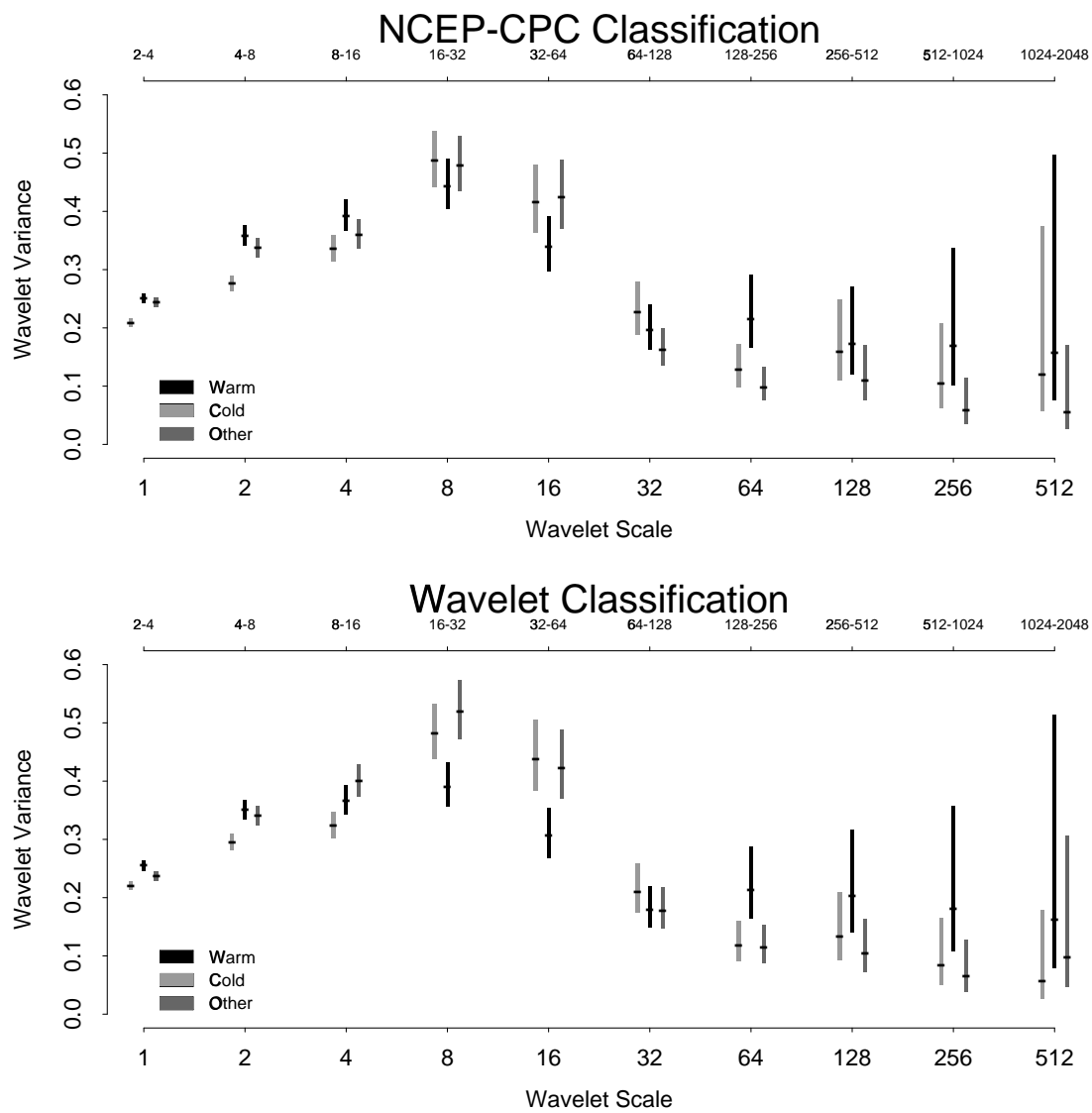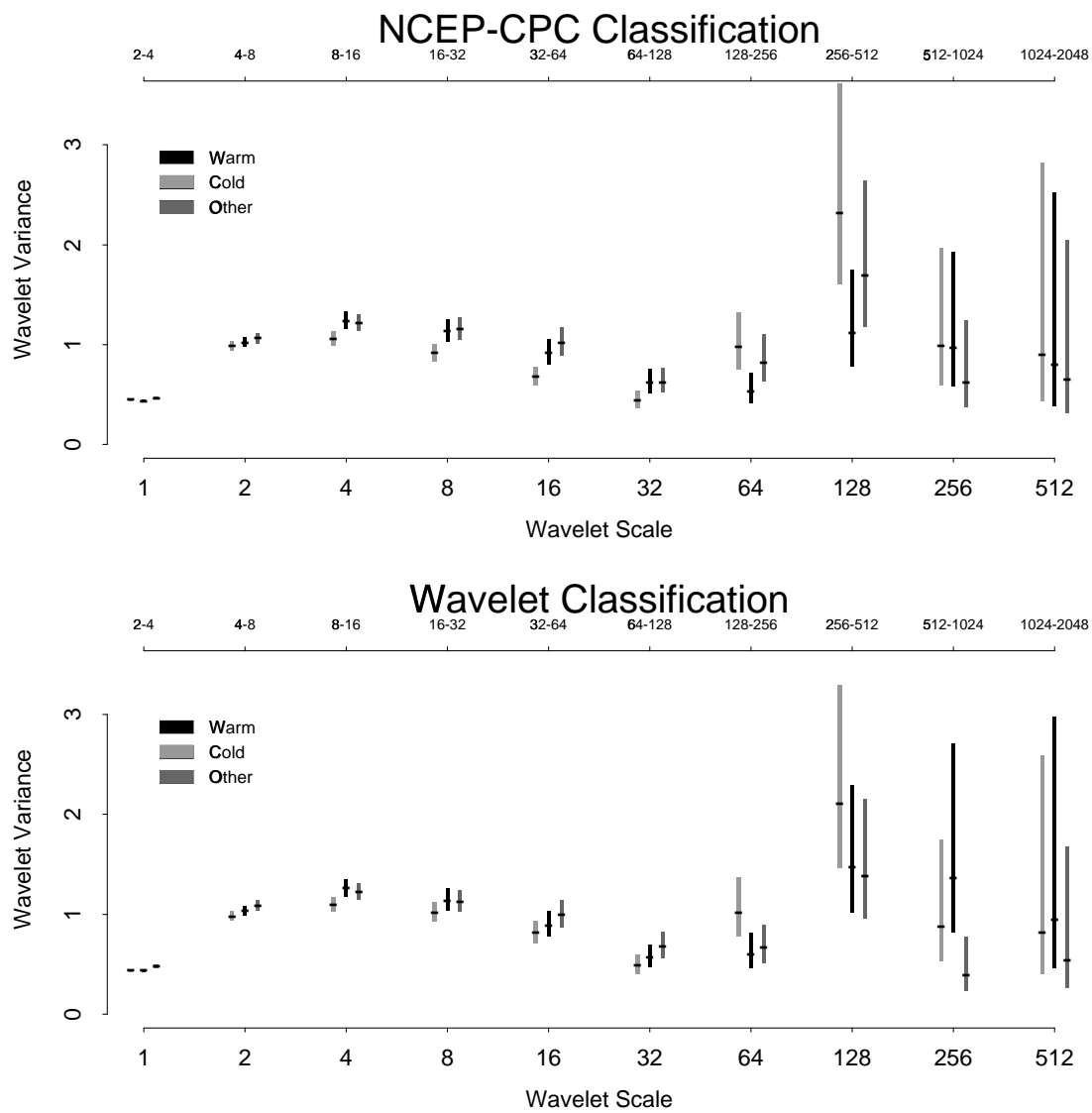time (years)
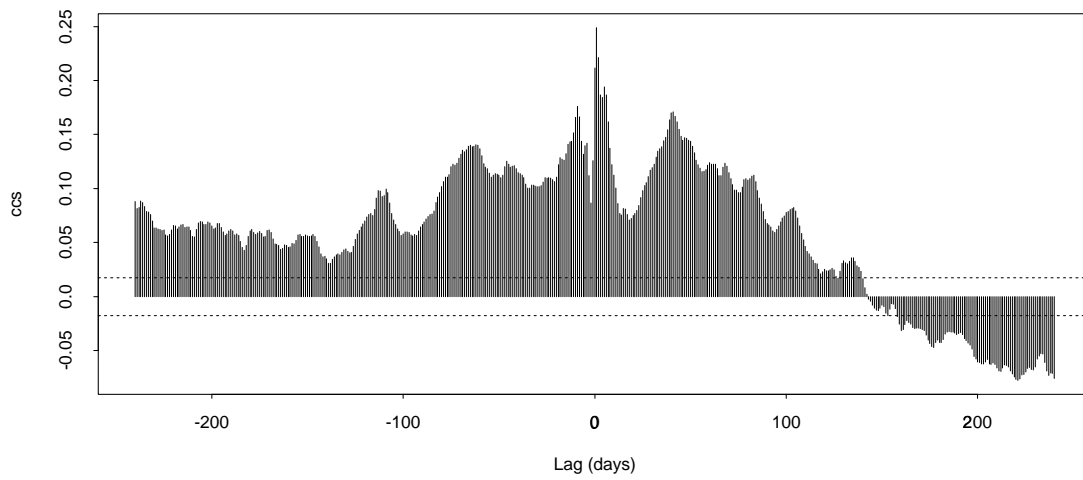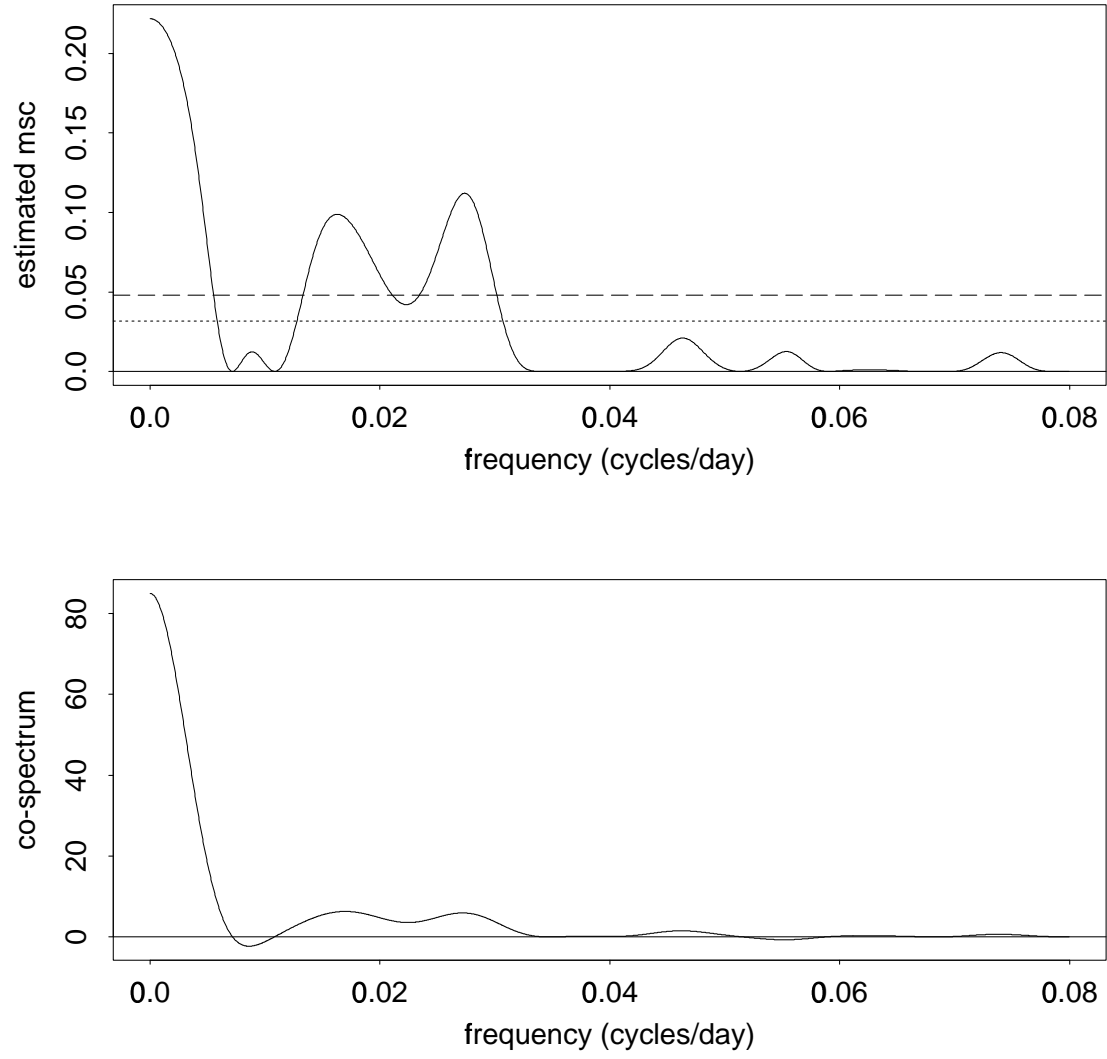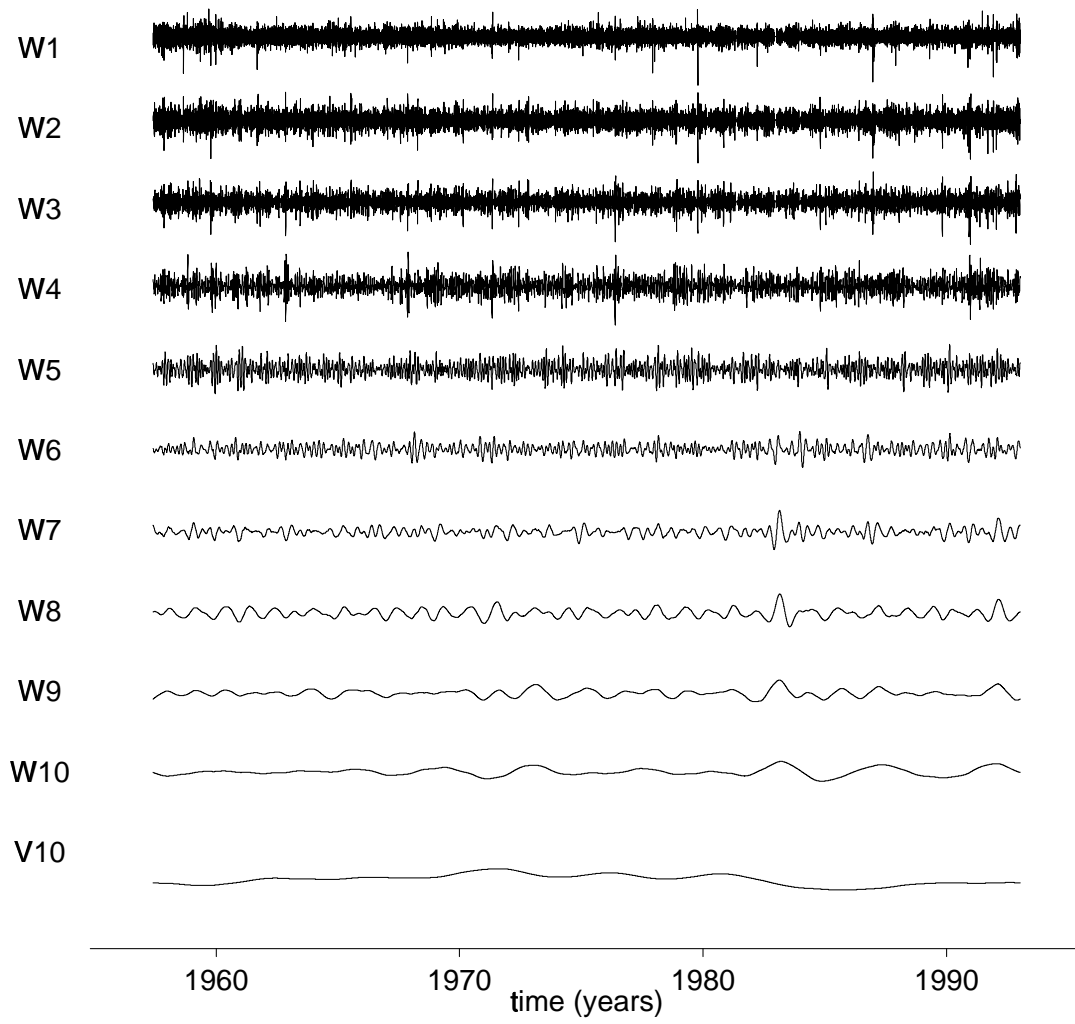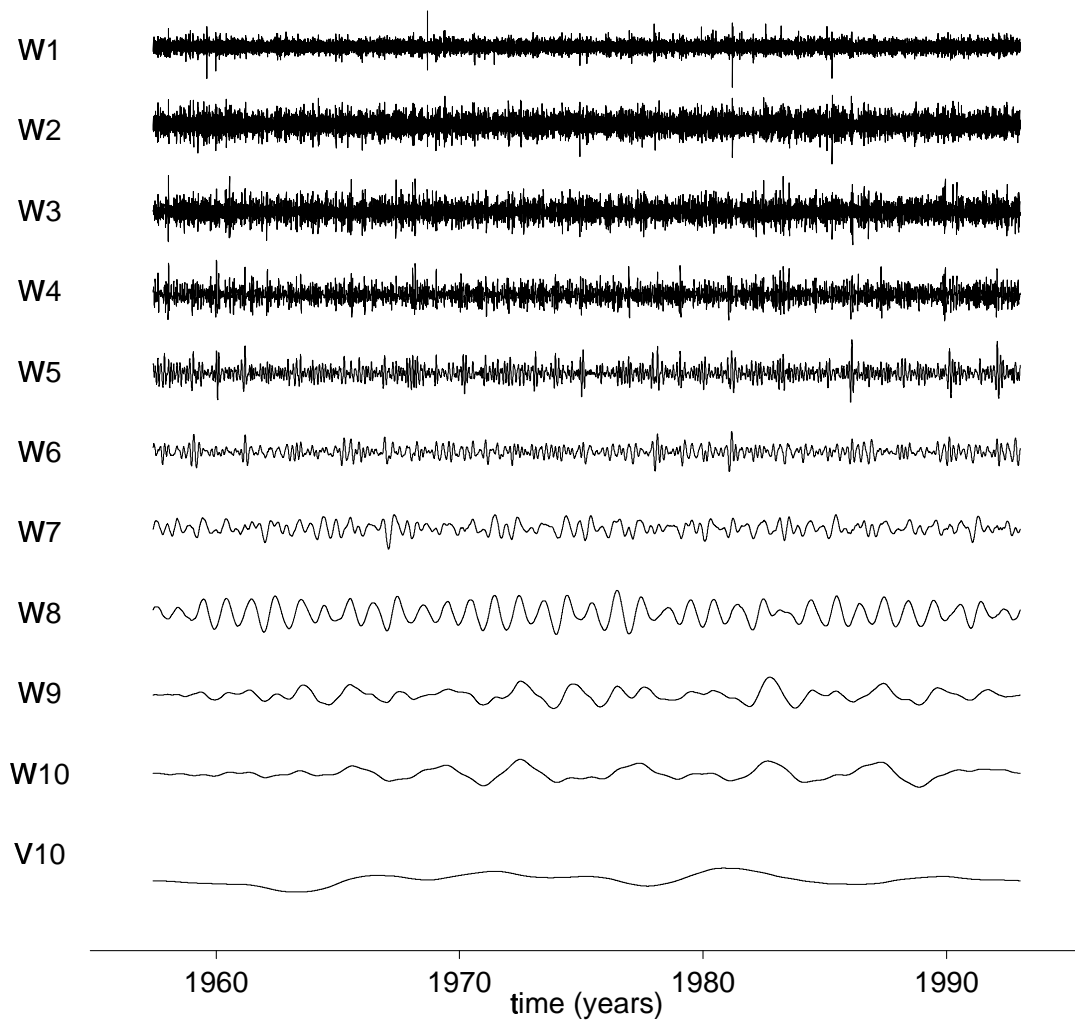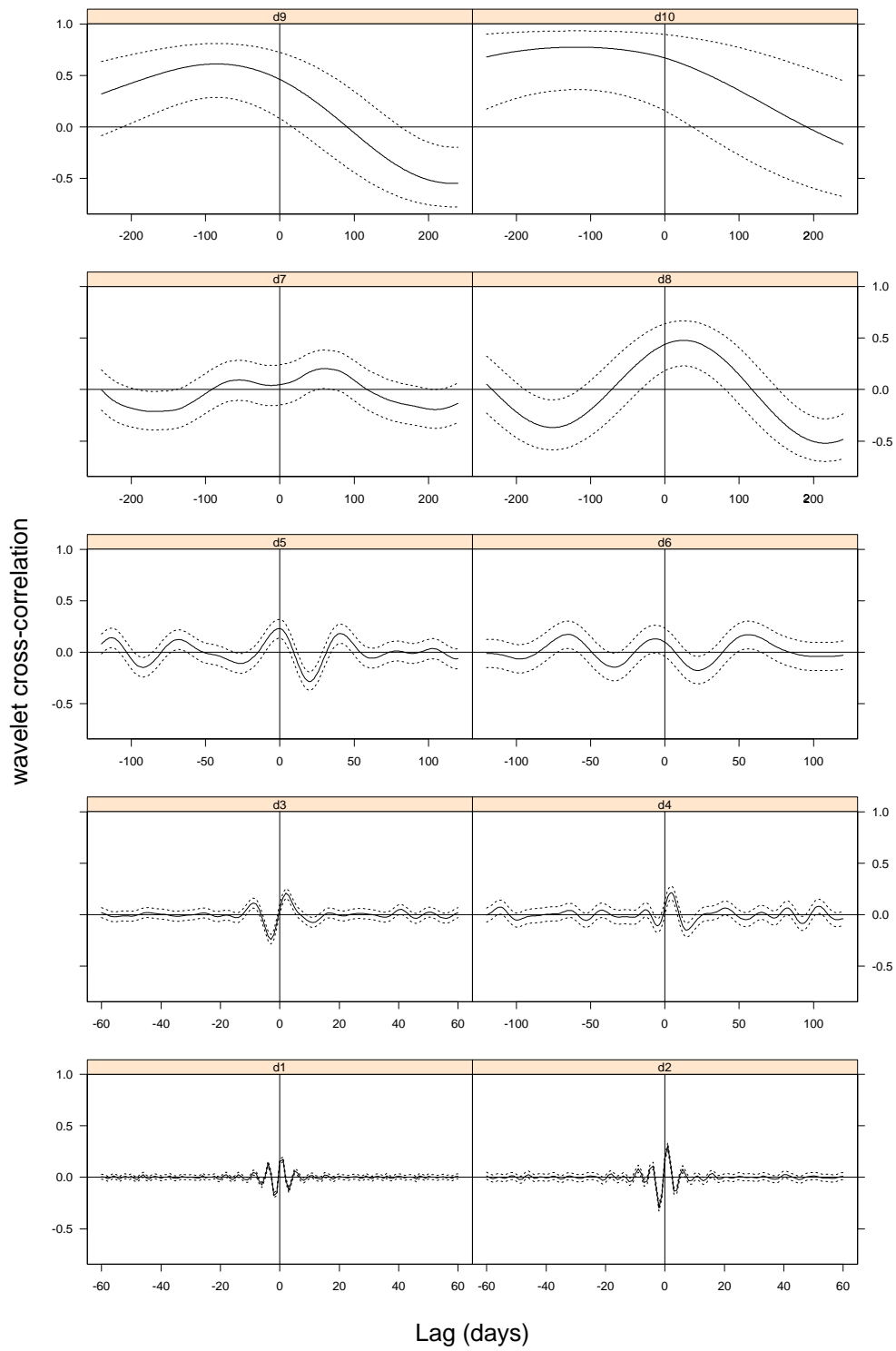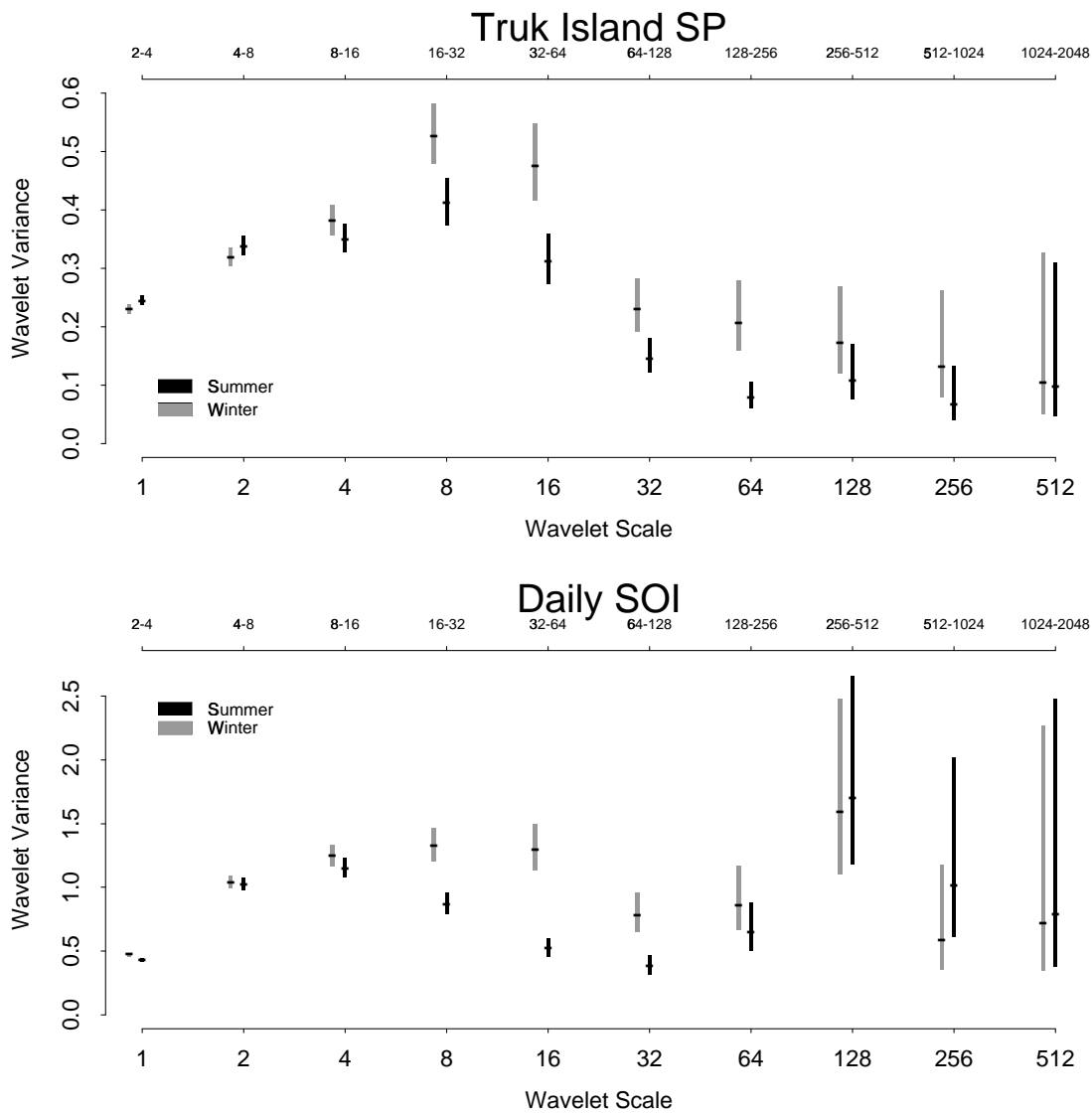
Figure 5.
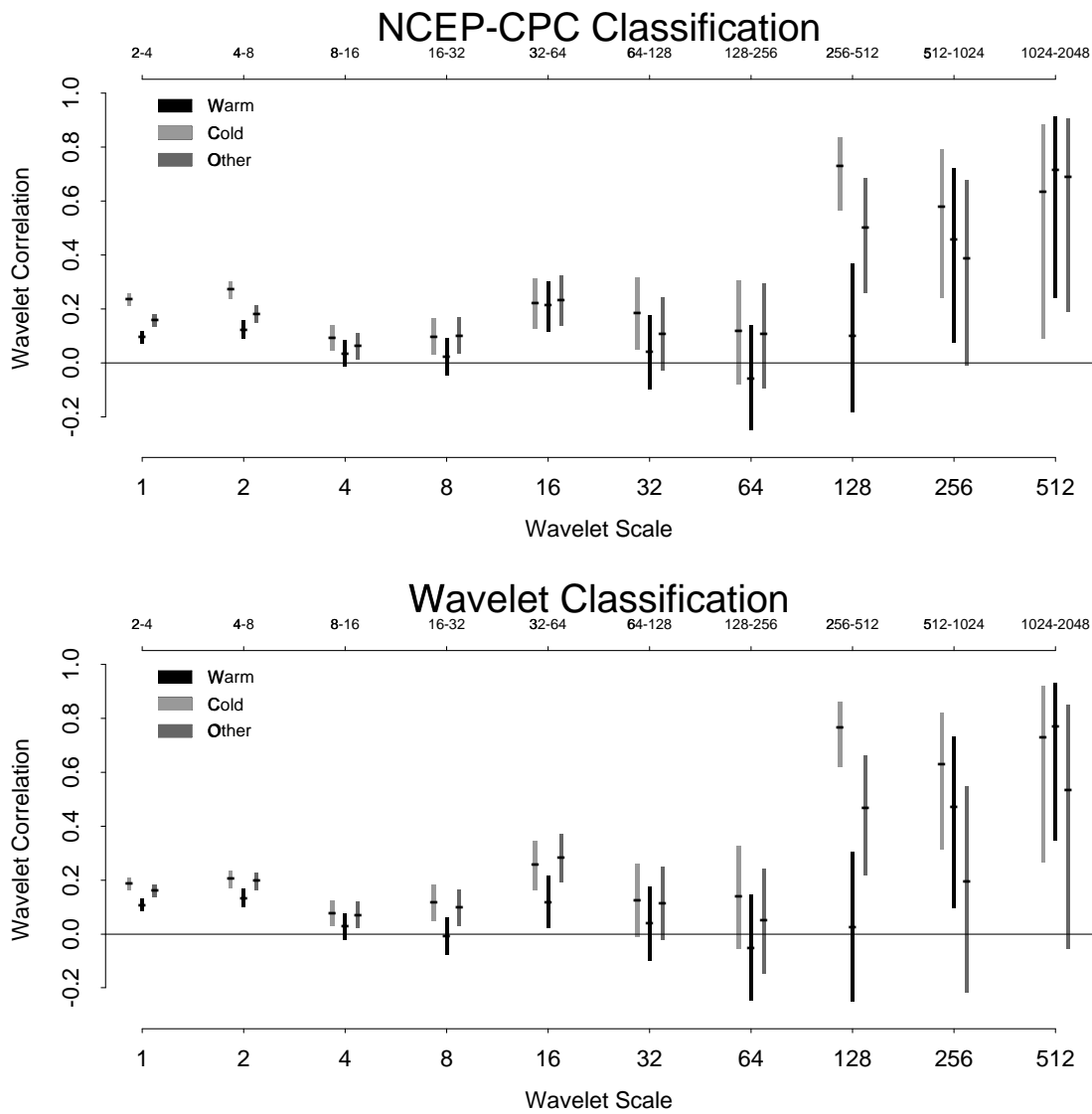
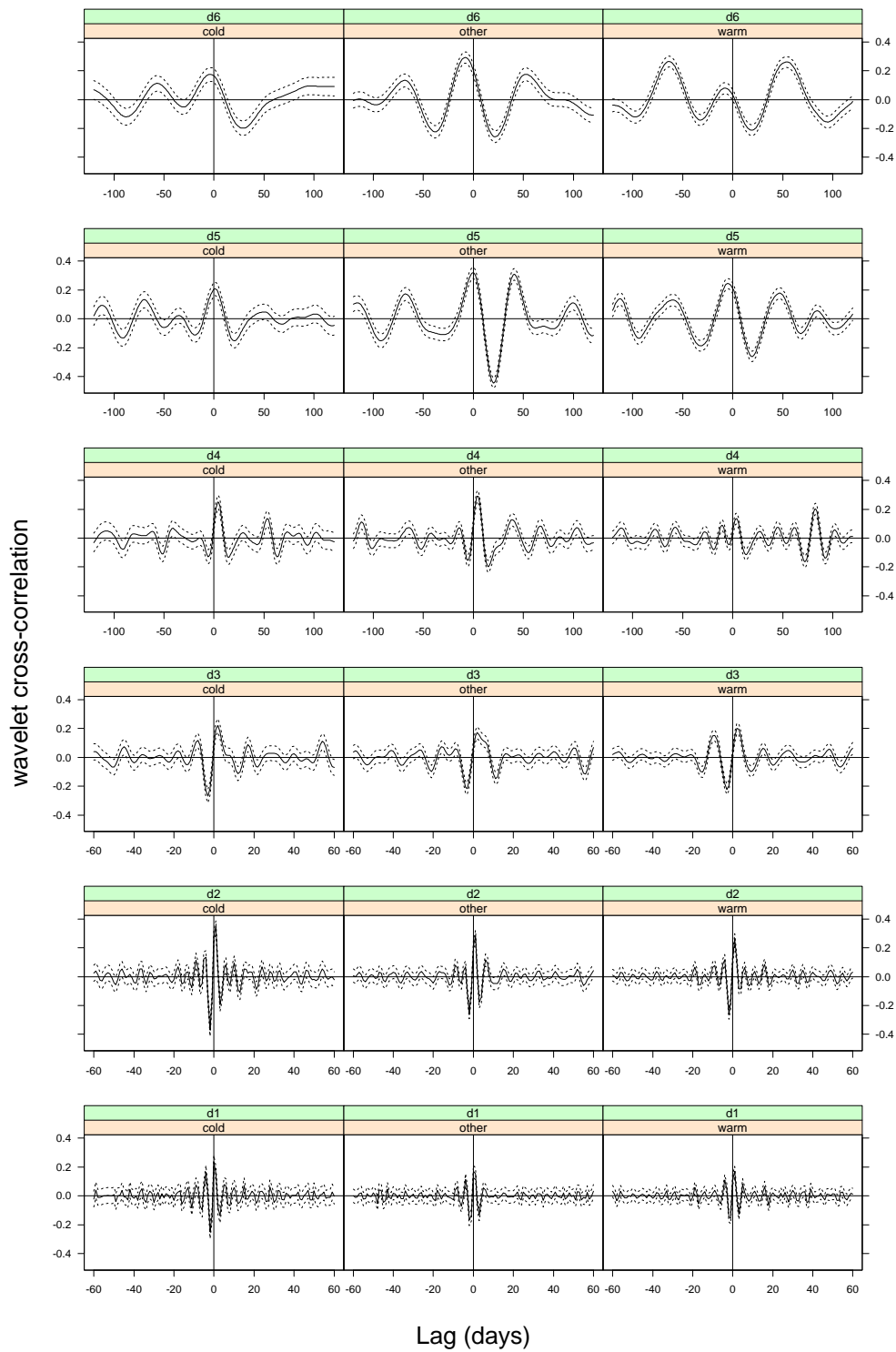Figure 6.

Figure 7.
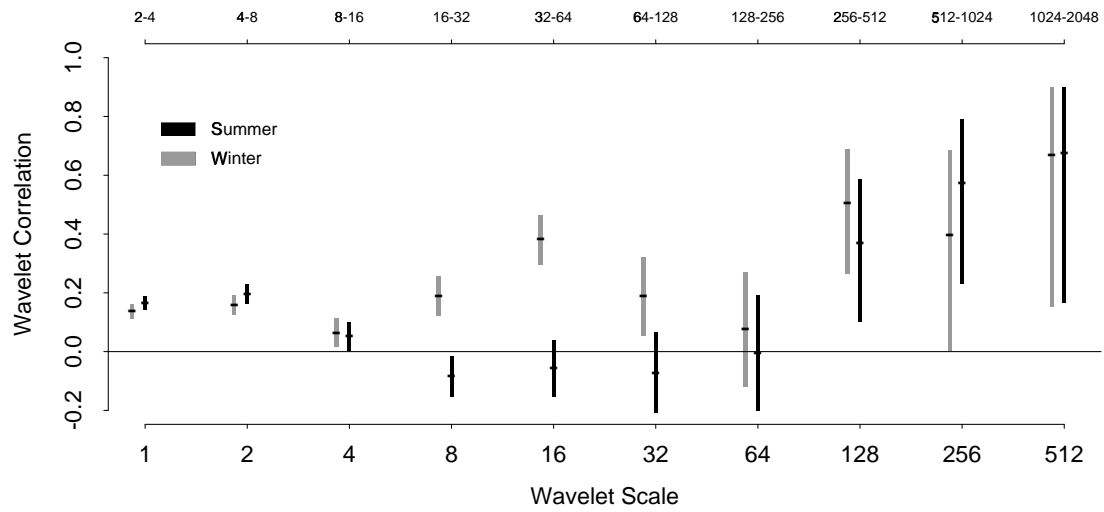
Figure 8.

Figure 9.

Figure 10.

Figure 11.

Figure 12.

Figure 13.

Figure 14.